symmetry

MDPI

Article

Hyperchaotic Maps and the Single Neuron Model: A Novel Framework for Chaos-Based Image Encryption

Wassim Alexan [1], Yen-Lin Chen [2,*], Lip Yee Por [3] and Mohamed Gabr [4]

1 Communications Department, Faculty of Information Engineering and Technology, German University in Cairo, Cairo 11835, Egypt; wassim.alexan@ieee.org
2 Department of Computer Science and Information Engineering, National Taipei University of Technology, Taipei 106344, Taiwan
3 Department of Computer System and Technology, Faculty of Computer Science and Information Technology, Universiti Malaya, Kuala Lumpur 50603, Malaysia; porlip@um.edu.my
4 Computer Science Department, Faculty of Media Engineering and Technology, German University in Cairo, Cairo 11835, Egypt; mohamed.gabr@ieee.org
* Correspondence: ylchen@mail.ntut.edu.tw

Abstract: With the explosion of the generation, transmission and sharing of image data over the Internet and other unsecured networks, the need for and significance of the development of novel image encryption algorithms are unprecedented. In this research work, we propose a novel framework for image encryption that is based on two hyperchaotic maps utilized in conjunction with the single neuron model (SNM). The framework entails three successive stages, where in every stage a substitution box (S-box) is applied, then XORing with an encryption key is carried out. The S-boxes and the encryption keys are generated from the numerical solutions of the hyperchaotic maps and the SNM. The performance of the proposed framework is gauged through a number of metrics, reflecting superior performance and complete asymmetry between the plain images and their encrypted versions. The main advantages of this work are (1) vast key space and (2) high encryption efficiency. The superior key space of 2^{2551} is the result of employing the two hyperchaotic maps, while the improved efficiency, resulting in an average encryption rate of 8.54 Mbps, is the result of using the SNM as well as the employment of optimized parallel processing techniques. In addition, the proposed encryption framework is shown to output encrypted images that pass the NIST SP 800 suite. Average achieved values for the metrics include MSE of 9626, PSNR of 8.3 dB, MAE of 80.99, entropy of 7.999, NPCR of 99.6% and UACI of 31.49%.

Keywords: cryptography; hyperchaotic maps; image encryption; NIST; S-box; single neuron model

check for updates

Citation: Alexan, W.; Chen, Y.-L.; Por, L.Y. ; Gabr, M. Hyperchaotic Maps and the Single Neuron Model: A Novel Framework for Chaos-Based Image Encryption. *Symmetry* **2023**, *15*, 1081. https://doi.org/10.3390/sym15051081

Academic Editors: Aniruddha Bhattacharjya and Remigiusz Wiśniewski

Received: 10 April 2023
Revised: 3 May 2023
Accepted: 11 May 2023
Published: 14 May 2023

1. Introduction

With the widespread use of digital images in various fields, including healthcare, finance and personal communication, there is a growing need to ensure their secure communication and storage. This is especially true in terms of protecting them from unauthorized access, tampering and interception [1,2]. Encryption is the process of converting plaintext (unencrypted data) into ciphertext (encrypted data) using an encryption algorithm and a secret key. The encrypted data can only be decrypted and read by someone who has the correct key. Image encryption is a specific type of encryption that is designed to protect digital images by eradicating any symmetry between a plain image and its encrypted version. The need for image encryption arises from several factors. Firstly, digital images often contain sensitive information, such as personal photos, medical images or confidential documents. This information needs to be protected from unauthorized access or interception during transmission over the Internet or storage on a device [3]. Secondly, images can be easily tampered with and it is often difficult to detect such tampering. Encryption can help prevent unauthorized modifications of the image data by providing a way to verify the authenticity of the image [4]. Thirdly, images are often stored and transmitted in large quantities, making it difficult to ensure the security of each individual image. Image encryption algorithms can help secure large quantities of images by providing a way to efficiently and securely process their data [5].

Recent literature shows the reliance of image encryption algorithms on substitution-permutation networks (SPNs). SPNs are a popular cryptographic primitive used in symmetric key encryption algorithms. These operate by applying a series of substitution and permutation operations to plaintext blocks, producing ciphertext blocks that are difficult for an attacker to decipher without the correct key. SPNs have been widely used in image encryption research due to their ability to efficiently encrypt large amounts of data while maintaining strong security guarantees [6–8]. In an image encryption algorithm, the plaintext is typically represented as a matrix of pixel values and the SPN is applied to each pixel value individually or to a block of pixels simultaneously. One of the main advantages of using SPNs in image encryption is their ability to provide a high degree of confusion and diffusion, satisfying Shannon's theory of secure communication [9]. Confusion refers to the property of the encryption algorithm that makes it difficult for an attacker to relate the ciphertext to the plaintext, while diffusion refers to the property that ensures that small changes in the plaintext lead to significant changes in the ciphertext [2].

SPNs have also been used in combination with other cryptographic techniques, such as key management and authentication, to provide a more comprehensive approach to image security [10]. For example, some image encryption algorithms based on SPNs use secret key management techniques to ensure that the encryption key is securely distributed and protected from unauthorized access [11]. Overall, the importance of SPNs in image encryption research lies in their ability to provide strong security guarantees while efficiently processing large amounts of data. As such, they have become a cornerstone of modern image encryption algorithms and continue to be an active area of research in the field of cryptography. In general, most recent literature on image encryption carries out confusion through the application of one or more substitution boxes (S-boxes), while diffusion is carried out through the application of an encryption key that is based on a pseudo-random number generated bitstream, where an appropriate logical operation is utilized [7,12,13]. The next couple of paragraphs introduce each of those steps.

Substitution boxes are an important component of many image encryption algorithms. These are used to substitute plaintext bits with ciphertext bits and they provide a key component of the confusion step in many encryption algorithms [7]. The importance of S-boxes in image encryption algorithms lies in their ability to provide strong security guarantees by introducing non-linear transformations into the encryption process. S-boxes help to ensure that changes to a single input bit have unpredictable and significant effects on the output, making it difficult for an attacker to analyze and reverse-engineer the encryption process. In image encryption, S-boxes are typically used in combination with permutation operations to form SPNs [12]. As mentioned, the SPN structure is particularly well-suited to image encryption because it provides a high degree of confusion and diffusion, which are both important properties for secure encryption. The use of S-boxes in image encryption algorithms can also help to prevent common attacks, such as differential and linear cryptanalysis, which rely on analyzing the statistical properties of the encryption process. S-boxes can help obscure these statistical properties, making it more difficult for an attacker to break the encryption [12].

Pseudo-random number generators (PRNGs) play an important role in image encryption algorithms. PRNGs are used to generate a sequence of random numbers that are used to encrypt the image data. These random numbers are combined with the original image data using various encryption techniques to produce encrypted image data that is difficult to decipher without the correct key [2]. The importance of PRNGs in image encryption algorithms lies in their ability to generate a large amount of unpredictable and uniformly distributed random numbers. These random numbers are crucial for achieving the two main goals of encryption: confidentiality and integrity [3]. Confidentiality refers to the property of the encryption algorithm that ensures that only authorized parties can access the encrypted data. Integrity refers to the property that ensures that the encrypted data has not been tampered with or modified during transmission or storage. PRNGs are designed to produce random numbers that are indistinguishable from true random numbers. However, unlike true random number generators, PRNGs are deterministic and rely on a seed value to produce the same sequence of numbers each time they are used with the same seed [12]. The seed value is typically generated from a source of true randomness, such as atmospheric noise, mouse movements or keyboard timings, to ensure that the resulting sequence of numbers is sufficiently unpredictable. In image encryption algorithms, PRNGs are used to produce a large sequence of random numbers that are combined with the original image data to produce encrypted data [2]. The strength and quality of the encryption depend on the randomness and uniformity of the PRNG output. Therefore, selecting a secure and robust PRNG is essential for ensuring the security and effectiveness of the image encryption algorithm.

Chaotic functions exhibit sensitive dependence on initial conditions and cycloidal behavior, making them suitable for encryption applications [6,8]. There are two main types: low-dimensional chaotic functions with two or three variables and hyperchaotic functions with four or more variables, thus spanning multiple dimensions and interacting in complex ways [14]. Low-dimensional chaotic functions, such as the Lorenz or Henon maps, have a smaller key space but simpler computational requirements, making them faster and easier to implement [13,15,16]. However, their lower dimensionality means they have weaker encryption strengths. Hyperchaotic functions, on the other hand, have a much larger key space due to their extra variables, providing stronger encryption. However, they also have greater complexity, requiring more computing power and being slower to compute. Each type has its advantages and disadvantages for image encryption. Low-dimensional chaos is suitable for real-time encryption of streaming videos or wireless communications due to its simplicity. Hyperchaos provides very high encryption strength, making it suitable for encrypting still images or large file transmissions. However, its added complexity may be impractical for some applications with limited resources. By tuning the parameters of a chaotic map, its dynamics can be made sufficiently random-like for encryption yet still deterministic for decryption [12]. Chaotic ciphers have been shown to withstand various attacks such as brute force, known plaintext and statistical analysis [12]. When combined with other techniques such as diffusion and confusion layers, chaos-based encryption schemes can achieve robust and versatile encryption of images and multimedia data [17]. Chaos provides an efficient and simple means of generating the complex, nonlinear transformations needed for strong encryption.

Recent literature in the field of image encryption provides a plethora of articles that combine the use of successive applications of PRNGs and S-boxes to carry out image encryption. In many instances, chaos theory is employed to generate the PRNGs and construct the S-boxes. In [12], the authors numerically solve the fractional-order hyperchaotic Chen system and generate a PRNG as an encryption key from its solution. They combine its use, in a multi-layer encryption algorithm, with other keys and S-boxes based on the Mersenne Twister, OpenSSL, Rule 30 cellular automata (CA) and Intel's math kernel library. The authors of [7] make use of a tan variation of the Logistic map to carry out Deoxyribonucleic acid (DNA) coding as a first stage of encryption. Subsequent stages utilize the Lorenz chaotic system to construct an S-box, as well as the Logistic map in its original form for PRNG key generation. Recaman's sequence, in conjunction with the Rossler chaotic system, is used to generate PRNG encryption keys in [18]. In [19], the authors employ chaotic functions, DNA computing, SHA-256, as well as the random movements of a chess piece, castle, on a hypothetical chess board, to carry out image encryption. The combination of DNA coding with chaos theory is also utilized in [20], where the authors further the image encryption abilities through SHA-2. A number of dynamical functions that exhibit chaotic behavior are utilized in [17] to generate PRNG encryption keys, including the linear congruential generator, the Arnold cat map, the Bernoulli map, the 2D Logistic sine map and the tent map. In [21], parameters are computed over the finite field Z_N through the utilization of a finite field with the aim of generalizing the Logistic map and searching for an auto morphic mapping between two Logistic maps, to carry out robust image encryption. The work of [15] adopts a continuous chaotic system, with the aim of achieving diffusion and an LA-semi group, with the aim of achieving confusion, for efficient image encryption. A 6D discrete hyperchaotic system is employed in [22] to generate six PRNGs as encryption keys. Those are used in conjunction with DNA coding, to encrypt each of the color-separated RGB channels of a color image. The authors of [23] make use of the spatio-temporal chaos of the 2D nonlinear coupled map lattices and genetic operations, to carry out low-complexity image encryption. The Mandelbrot set is utilized in a color image encryption scheme proposed in [24], where the Arnold map combined with DNA sequences enhances the attained encryption security. The authors of [25] propose an innovative image encryption algorithm that draws on the distinctive concept of a rotor machine, in addition to the employment of a piece-wise linear chaotic map and a one-time key. The Logistic map is used in combination with a dynatomic modular curve, as a form of an SPN, to perform secure image encryption in [26]. In [27], the authors employ a cloud model, a Fibonacci chaotic system and a matrix convolution operation to implement a secure image cryptosystem. Interesting work involving the Josephus problem and its corresponding Josephus function is employed in [28] in combination with a 4D hyperchaotic function. Image compression and encryption is carried out in [29], where the Arnold map and Choas theory are utilized for effective and reliable image transmission over unsecured networks. The authors of [30] devise a novel chaotic map, the Salomon map and showcase its superior chaotic behavior, in terms of positive and large Lyapunov exponents, then they employ its use in image encryption in conjunction with a pixel-splitting algorithm. Another novel chaotic map is introduced in [31], where the authors conceive a Schaffer map for high complexity applications. In their work, they compare the Schaffer map with counterparts from the literature and showcase that it has the best ergodicity and erraticity characteristics. Next, they illustrate its use in generating encryption keys and apply it to carrying out permutation and diffusion in a simple image encryption algorithm. In [32], the authors focus on improving encryption efficiency. This is carried out by designing a parallel image encryption algorithm using intra bitplane scrambling. In their proposed scheme, multiple processing threads are employed to carry out image encryption at the bit-level to achieve permutation. Next, every thread scrambles two bitplanes.

It is clear from the literature review that there are an abundance of techniques and algorithms that may be utilized to successfully implement secure, robust and efficient image encryption frameworks. However, almost all of the mentioned algorithms are only able to offer two of those three vital encryption traits. Such that the offering of higher security, through more encryption stages, is counteracted with higher design complexity and software implementations. In some cases, efficiency is capitalized on, but security is not fully achieved, such that key spaces are rather small. In order to achieve all three traits of security, robustness and efficiency, this work proposes and accomplishes the following:

- A chaos-based, three-stage, dual-acting image encryption framework is proposed. In every stage, a novel S-box is constructed and applied. This is followed by the generation and application of the logical XOR operation between a generated PRNG key and the image bits.
- In the first stage, a 7D hyperchaotic system of differential equations is numerically solved and its solution is utilized both for PRNG key generation and S-box construction.
- In the second stage, a single neuron model is numerically solved and its solution is utilized both for PRNG key generation and S-box construction.
- In the third stage, a 4D hyperchaotic system of differential equations is numerically solved and its solution is utilized both for PRNG key generation and S-box construction.
- With the utilization of three different systems, two of which are hyperchaotic, as well as the selection of three S-boxes that satisfy certain criteria, a rather wide key space of 2^{2551} is achieved, providing sufficient resistivity to brute-force attacks.

- The software implementation of the proposed image encryption framework making use of advanced parallel processing techniques allows for an average encryption rate of 8.54 Mbps to be achieved.

This article is organized as follows. Section 2 makes reference to the foundational systems of differential equations that are to be employed for PRNG key generation and outlines the adopted methodology for the construction of S-boxes. Section 3 introduces the image encryption and decryption processes of the proposed framework. Section 4 provides the numerical results and performance evaluation of the proposed framework. A comparative study of the state-of-the-art is also carried out in this section. Section 5 concludes this research work and provides some suggestions for possible future areas of research.

2. Preliminary Mathematical Constructs

A number of mathematical constructs are used in the proposed image encryption framework to generate the PRNG keys and S-boxes. These are presented in this section.

2.1. The Single Neuron Model

The single neuron model (SNM) is a mathematical model that describes the behavior of a single neuron with an adaptive feedback synapse. The model consists of two differential equations: one that describes the membrane potential of the neuron and one that describes the dynamics of the feedback synapse. The authors of [33] have shown that an SNM with an adaptive feedback synapse has two coexisting chaotic attractors. In this work, we make use of this SNM because of its rich, complex dynamics and its suitability with respect to inducing randomness in a simple and deterministic manner. The SNM is described as follows:

$$\begin{cases} \dot{u} = -\dfrac{u}{\tau} + f(qs)f(pu) + I, \\ \dot{s} = -\alpha s + \alpha f^2(pu), \end{cases} \tag{1}$$

where $\alpha = 1/B$, while p and q are positive constants. As in [33], $f(x) = 3xexp(-x^2/2)$ (shown in Figure 1), while $I(t) = \epsilon sin(\omega t)$. The connected chaotic attractor of this system is plotted in Figure 2 for $\alpha = 3$, $u_0 = 0.1$ and $s_0 = 0.5$. In Figure 2, the colors model the time factor representing initiations with cold colors and endings with hot colors. In [33], bifurcation diagrams are provided for the SNM, confirming its chaotic behavior; however, a Lyapunov exponents plot is not provided, so we provide such a plot in Figure 3. It is clear from Figure 3 that two Lyapunov exponents materialize and one of them is positive.

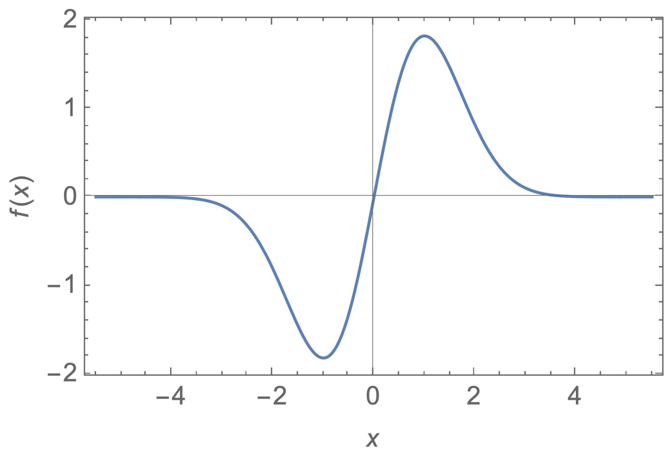

Figure 1. A plot of $f(x) = 3xexp(-x^2/2)$.

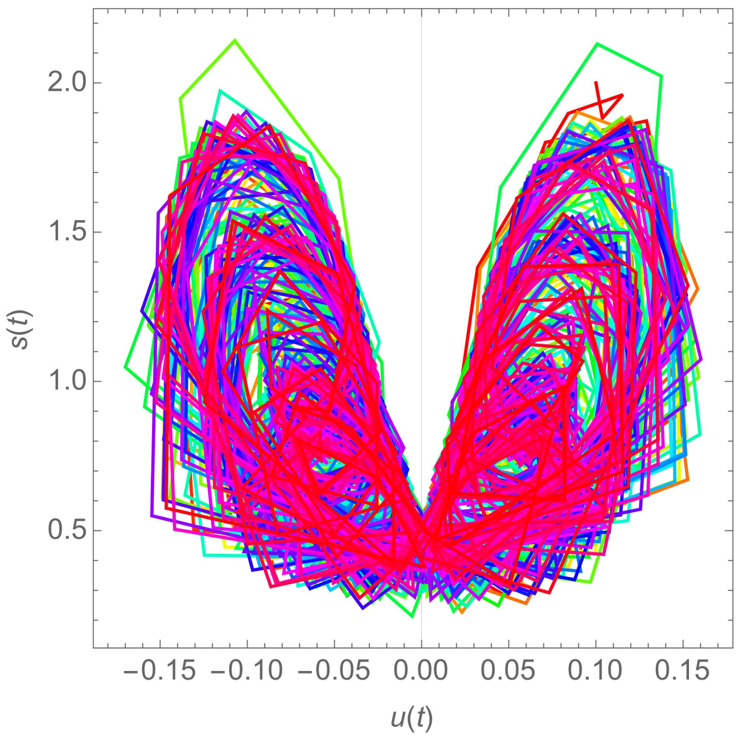

Figure 2. The connected chaotic attractor for the SNM at $\alpha = 3$.

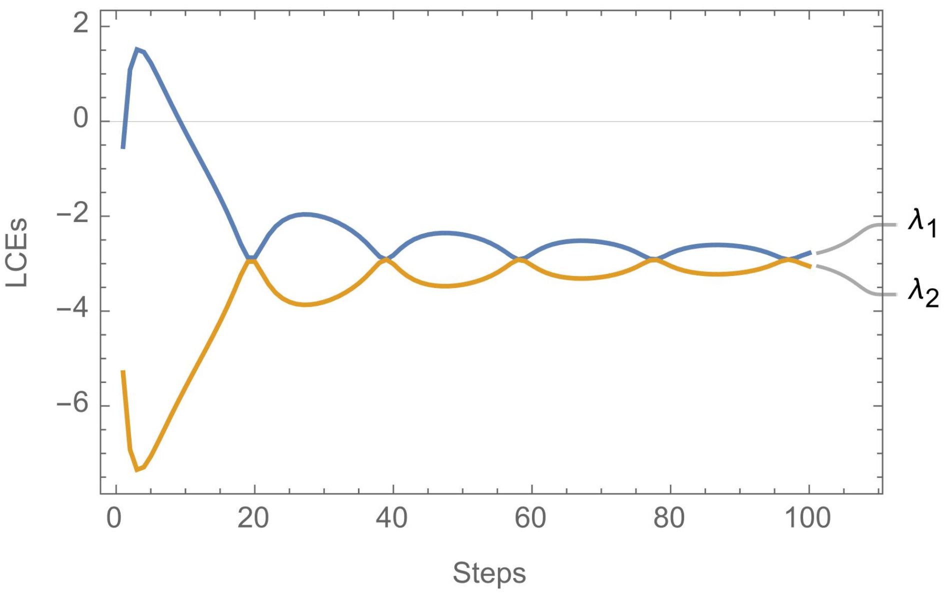

Figure 3. Lyapunov exponent plot for the SNM at $\alpha = 3$.

2.2. The 4D Hyperchaotic System

A 3D hyperchaotic system was proposed for the first time by the authors of [34]. This system was later improved by the authors of [35], who added a linear controller, resulting in the following 4D system of differential equations:

$$\begin{cases} \dot{u} = a(v-u) + evw, \\ \dot{v} = cu + dv - uw + mp, \\ \dot{w} = -bw + uv, \\ \dot{p} = -ku - kv, \end{cases} \tag{2}$$

where u, v, w and p are the states of the system and a, b, c, d, e, m, k are positive real parameters of the system and $c \in \mathbb{R}$. By letting $a = 15, b = 43, c = -1, d = 16, e = 5, m = 5$ and varying k, such that $k \in [1.5, 5.5]$, the authors of [35] show that the system in (2) possesses hyperchaotic attractors (shown for various spaces in Figure 4) and two positive Lyapunov exponents, providing the related plots that justify their claims (see Figure 1 for the Lyapunov exponents and Figure 2 for the bifurcation diagram, in [35]). In relation to image encryption, these properties make this system a good choice for utilization in PRNG generation and subsequent S-box construction. Furthermore, as a 4D system, the system in (2) has a large number of states and parameters, which allows it to provide an excellent expansion to the key space of the proposed image encryption framework.

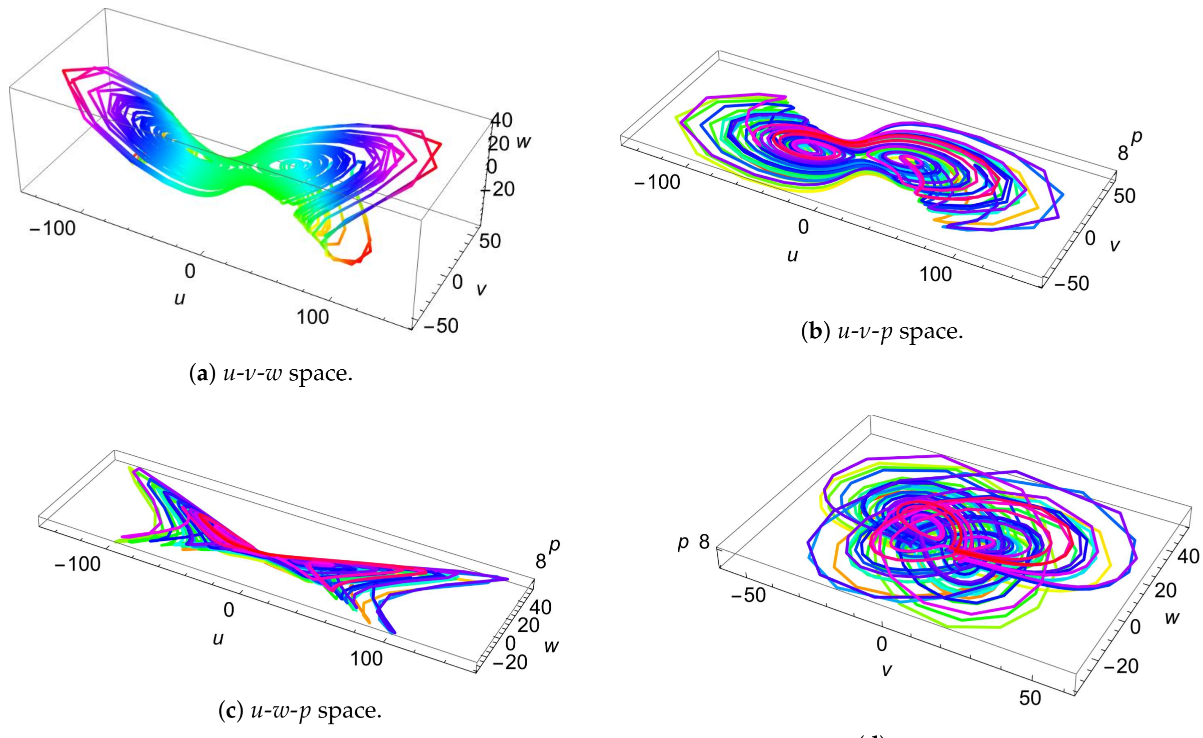

(**a**) u-v-w space. (**b**) u-v-p space. (**c**) u-w-p space. (**d**) v-w-p space.

Figure 4. Hyperchaotic attractors for system (2) with $u_0 = 5.2, v_0 = 7.4, w_0 = 1.4, p_0 = 3.4$, shown for various 3D spaces.

2.3. The 7D Hyperchaotic System

The authors in [36] presented a 7D hyperchaotic system. In their work, they propose coupling the classical Lorenz 3D system with a 6D hyperchaotic system. This 6D system is obtained through the addition of a nonlinear feedback controller to the first equation and a linear feedback controller to the second equation of the classical Lorenz 3D system. Such coupling results in a novel 7D hyperchaotic system as follows:

$$\begin{cases} \dot{x_1} = a(x_2 - x_1) + x_4 + bx_6, \\ \dot{x_2} = cx_1 - x_2 - x_1x_3 + x_5, \\ \dot{x_3} = -dx_3 + x_1x_2, \\ \dot{x_4} = ex_4 - x_1x_3, \\ \dot{x_5} = -fx_2 + x_6, \\ \dot{x_6} = gx_1 + hx_2, \\ \dot{x_7} = lx_7 + mx_4, \end{cases} \tag{3}$$

where $x_i, i \in [1, 7]$ are the states of the system and $a, b, c, d, e, f, g, h, l$ and m define its parameters. The following set of values for the parameters allows the system in (3) to have seven Lyapunov exponents of which five are positive: $(a, b, c, d, e, f, g, h, l, m) = (10, 8/3, 28, 2, 9.9, 1, 2, 1, 1, 1)$. Figure 5 displays the hyperchaotic attractors of this 7D system. While the system in (3) is shown to have a rather simple algebraic structure, nevertheless it exhibits complex dynamical behaviors due to possessing five positive Lyapunov exponents. The authors in [36] provide the related plots that justify their claims (see Figure 6 for the Lyapunov exponents and Figure 7 for the bifurcation diagram, in [36]). In relation to image encryption, these properties make this system a good choice for utilization in PRNG generation and subsequent S-box construction. Furthermore, being a 7D system, it has a large number of states and parameters, which allows it to provide an excellent expansion to the key space of the proposed image encryption framework.

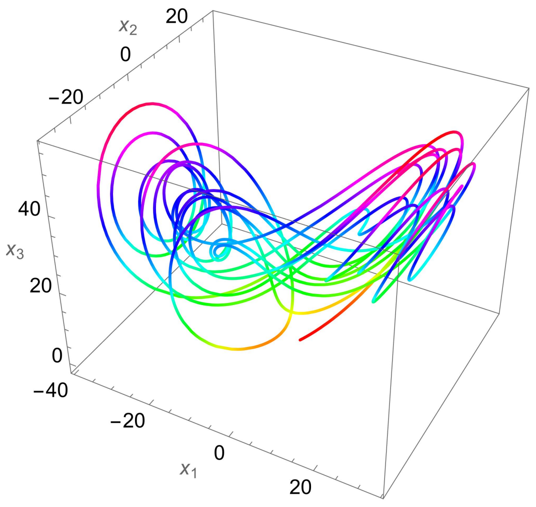

(**a**) x_1-x_2-x_3 space.

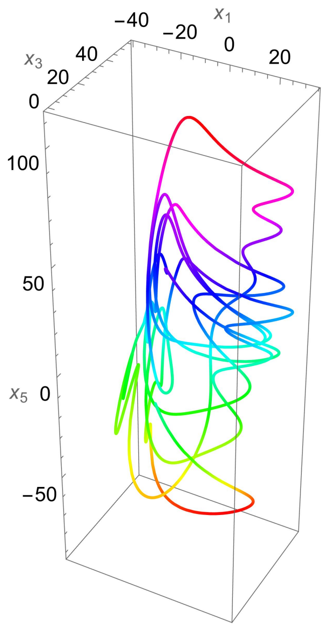

(**b**) x_1-x_3-x_5 space.

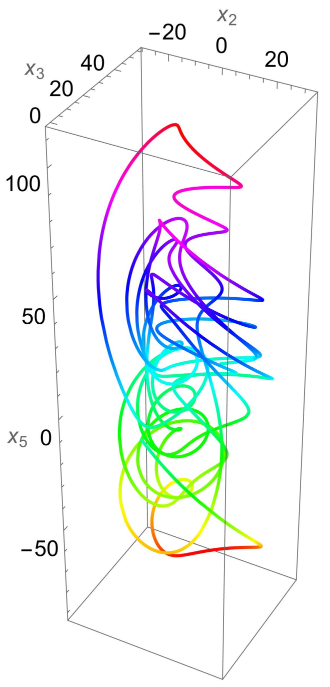

(**c**) x_2-x_3-x_5 space.

Figure 5. *Cont.*

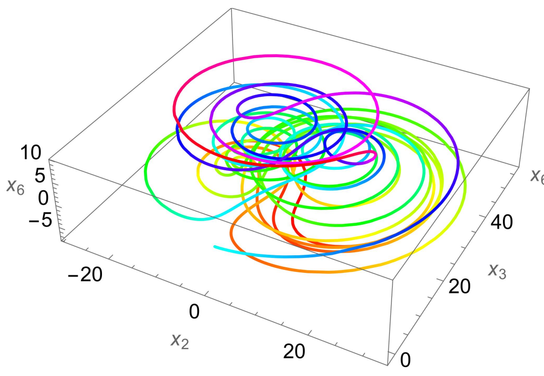

(**d**) x_2-x_3-x_6 space.

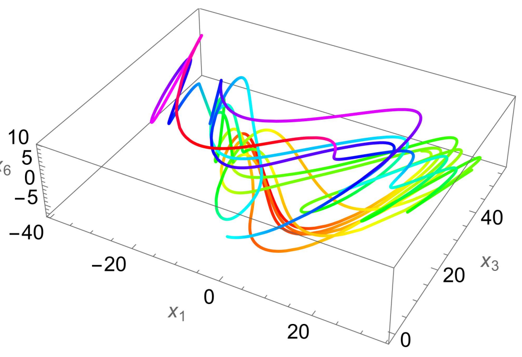

(**e**) x_1-x_3-x_6 space.

Figure 5. Hyperchaotic attractors for system (3) with $(a, b, c, d, e, f, g, h, l, m) = (10, 8/3, 28, 2, 9.9, 1, 2, 1, 1, 1)$, shown for various 3D spaces.

2.4. S-Box Construction

In this work, the main aim of the S-box construction process is to involve the S-box evaluations in the generation process. In other words, the numerical values produced by the techniques used in evaluating the performance of S-boxes are utilized as part of the key space of the S-box generation step (which is reflected in the overall key space of the proposed image encryption framework). Moreover, the process adopted here makes use of the generated PRNG bitstreams discussed in Sections 2.1 through 2.3. Accordingly, two mechanisms are applied to achieve that, with one of them being a sub-routine to the other.

Starting with the inner process, the aim is to transform a bit stream of length 2048 into an S-box. This is performed by, first, converting the 2048 bits into 256 integers. As these integers are randomly generated, they are expected to be unsorted and to contain duplicates. Hence, this set of integers is utilized as a selection function applied to a sorted set [0–255], where the selected element from the set is removed. Therefore, the selected integers are re-adjusted to the length of the sorted set using the modulus operator. As a result of the selection and the re-adjustment processes being applied sequentially, values are shifted from the sorted set (which descends in size) into the S-box, generating an S-box by the time the length of the sorted set reaches 0.

Based on the inner process discussed above, the role of the outer process is to generate a set of S-boxes, evaluate each one individually and select the S-box with performance evaluation values closest to a provided set of values. In consequence, a bitstream of size $2048 \times n$ is needed as an input, such that n is the number of S-boxes to be generated and evaluated, and from which one is selected. Given such input, the bitstream is partitioned into sections of length 2048, transformed into S-boxes (using the inner process) and evaluated and the performance evaluation values are subtracted from the given target evaluations yielding the S-box with the smallest difference.

3. Proposed Image Encryption Framework

The encryption process is described in Section 3.1, while the decryption process is described in Section 3.2. Section 3.3 presents algorithms that are employed as part of the encryption and decryption processes.

3.1. The Encryption Process

The following sequence of steps outlines the proposed three-stage encryption process.

1. A color image I of length M and width N is chosen and the pixel values of its RGB channels are arranged as a single bitstream d, of length L_d, where:

$$L_d = M \times N \times 3 \times 8. \tag{4}$$

2. Encryption stage 1: The 7D hyperchaotic system encryption key and S-box.

(a) The 7D hyperchaotic system is numerically solved for the S-box seeds, then the numerical solution is utilized in Algorithm 1, resulting in an S-box S_{HC7D} (shown in Table 1).

Table 1. Seven-dimensional hyperchaotic system based S-box.

30	62	124	248	235	148	35	202	143	22	43	85	170	76	161	48
129	2	253	231	190	93	153	60	50	100	198	75	151	11	61	212
4	228	167	111	220	142	13	89	210	118	237	168	25	51	101	197
174	38	78	152	54	41	17	65	105	183	29	64	112	215	94	214
10	125	74	56	16	242	136	6	122	147	132	251	146	28	18	34
69	130	95	217	52	102	191	126	113	79	0	119	223	40	82	141
3	120	236	109	162	159	137	115	45	177	239	222	86	171	63	186
241	21	42	200	175	123	12	68	110	234	218	145	221	199	149	24
47	91	179	88	157	55	140	255	14	250	213	138	194	66	58	108
207	131	172	70	165	71	187	44	240	107	243	227	67	182	232	211
7	23	32	73	133	184	163	173	98	192	117	230	208	158	128	225
196	81	144	9	33	247	39	169	185	104	77	31	164	114	229	204
189	103	226	166	57	46	96	249	15	178	181	155	49	106	244	209
26	201	135	20	139	246	238	245	180	176	156	72	193	116	84	83
252	254	195	53	27	134	205	87	97	219	127	150	121	99	188	154
160	37	216	80	224	19	233	59	1	90	206	36	203	8	5	92

(b) A replacement process is applied to the image I, employing S_{HC7D} and resulting in image I_{11}.

$$I_{11} = S_{HC7D}(I). \tag{5}$$

(c) The pixels of the encrypted image I_{11} are transformed into a 1D bitstream d_{11}.

(d) The 7D hyperchaotic system is numerically solved for the key seeds. Algorithm 2 is utilized to generate an encryption key k_{HC7D} from the obtained solution, such that the length of this key is equal to L_d.

(e) The plaintext bitstream d_{11} is XORed with the encryption key k_{HC7D}.

$$d_{12} = d_{11} \oplus k_{HC7D}. \tag{6}$$

(f) The resulting bitstream d_{12} is transformed back into an image I_{12}.

3. Encryption stage 2: The single neuron model encryption key and S-box.

(a) The single neuron model is numerically solved for the S-box seeds, then the numerical solution is utilized in Algorithm 1, resulting in an S-box S_{SNM} (shown in Table 2).

(b) A replacement process is applied to image I_{12}, employing S_{SNM}, resulting in image I_{21}.

$$I_{21} = S_{SNM}(I_{12}). \tag{7}$$

(c) The pixels of the encrypted image I_{21} are transformed into a 1D bitstream d_{21}.

(d) The single neuron model is numerically solved for the key seeds. Algorithm 2 is utilized to generate an encryption key k_{SNM} from the obtained solution, such that the length of this key is equal to L_d.

Table 2. SNM-based S-box.

36	119	247	239	72	35	152	117	47	126	236	87	11	241	183	98
67	15	61	127	90	217	198	139	159	106	167	101	177	197	20	170
163	109	165	99	235	173	216	134	26	238	17	16	34	229	110	212
69	150	196	86	180	115	192	209	146	203	223	95	22	137	120	71
189	129	74	154	114	200	246	80	6	46	214	59	97	65	77	176
108	62	224	14	213	29	226	172	242	0	89	84	195	33	4	23
118	245	116	252	174	96	40	48	240	148	227	54	78	164	38	104
131	64	205	100	142	52	169	215	178	157	51	66	222	237	91	37
138	30	207	123	234	149	221	219	230	50	175	155	141	125	12	92
60	187	251	8	93	105	83	179	121	41	181	171	5	124	19	225
250	185	166	85	112	130	10	228	73	42	18	253	190	79	7	249
220	147	218	156	248	161	107	182	94	53	208	82	136	13	133	63
145	231	31	143	135	202	255	2	43	56	28	103	199	201	232	70
39	122	1	160	58	111	233	194	44	206	210	24	193	76	211	191
49	88	102	244	27	45	57	81	188	254	32	128	153	3	68	204
21	132	243	140	151	113	55	168	25	75	144	184	162	186	9	158

(e) The bitstream of the encrypted image d_{21} is XORed with the encryption key k_{SNM}.

$$d_{22} = d_{21} \oplus k_{SNM}. \tag{8}$$

(f) The resulting data bits d_{22} are transformed back into an image I_{22}.

4. Encryption stage 3: The 4D hyperchaotic system encryption key and S-box.

(a) The 4D hyperchaotic system is numerically solved for the S-box seeds, then the numerical solution is utilized in Algorithm 1, resulting in an S-box S_{HC4D} (shown in Table 3).

(b) A replacement process is applied to image I_{22}, employing S_{HC4D} and resulting in image I_{31}.

$$I_{31} = S_{HC4D}(I_{22}). \tag{9}$$

(c) The pixels of the encrypted image I_{31} are transformed into a 1D bitstream d_{31}.

(d) The 4D hyperchaotic system is numerically solved for the key seeds. Algorithm 2 is utilized to generate an encryption key k_{HC4D} from the obtained solution, such that the length of this key is equal to L_d.

(e) The bitstream of the encrypted image d_{31} is XORed with the encryption key k_{HC4D}

$$d_{32} = d_{31} \oplus k_{HC4D}. \tag{10}$$

(f) The resulting data bits d_{32} are transformed back into an image I_{32}. $I' = I_{32}$ is the final output encrypted image.

A flow chart illustrative of the proposed three-stage encryption process is provided in Figure 6.

Table 3. Four-dimensional hyperchaotic system-based S-box.

87	103	129	234	78	114	219	70	90	239	108	223	106	135	133	116
107	91	229	79	71	3	122	83	8	240	17	148	2	150	55	1
32	35	22	137	204	97	16	136	52	27	220	58	202	217	43	218
138	54	157	53	46	80	81	59	60	232	248	215	161	251	62	152
227	235	164	163	177	226	73	23	186	191	120	38	112	246	95	172
101	1	11	72	160	25	15	126	47	6	253	100	183	24	216	39
7	19	26	93	194	67	10	149	140	99	171	154	88	77	132	228
48	225	128	243	245	12	254	139	184	49	5	151	42	44	145	66
34	185	65	82	221	189	36	175	244	213	130	30	69	144	236	142
9	29	197	28	165	115	188	41	74	76	196	110	61	155	211	124
75	238	89	181	252	222	98	237	241	63	121	224	85	212	199	131
57	143	4	51	84	167	105	190	173	203	141	198	207	200	176	174
179	214	242	20	195	205	192	14	111	134	119	230	96	33	170	18
146	158	68	123	127	94	250	31	206	169	147	168	180	64	92	40
178	231	255	56	37	193	182	156	208	117	201	21	109	118	166	153
187	50	45	104	102	162	209	247	233	125	113	249	159	86	0	210

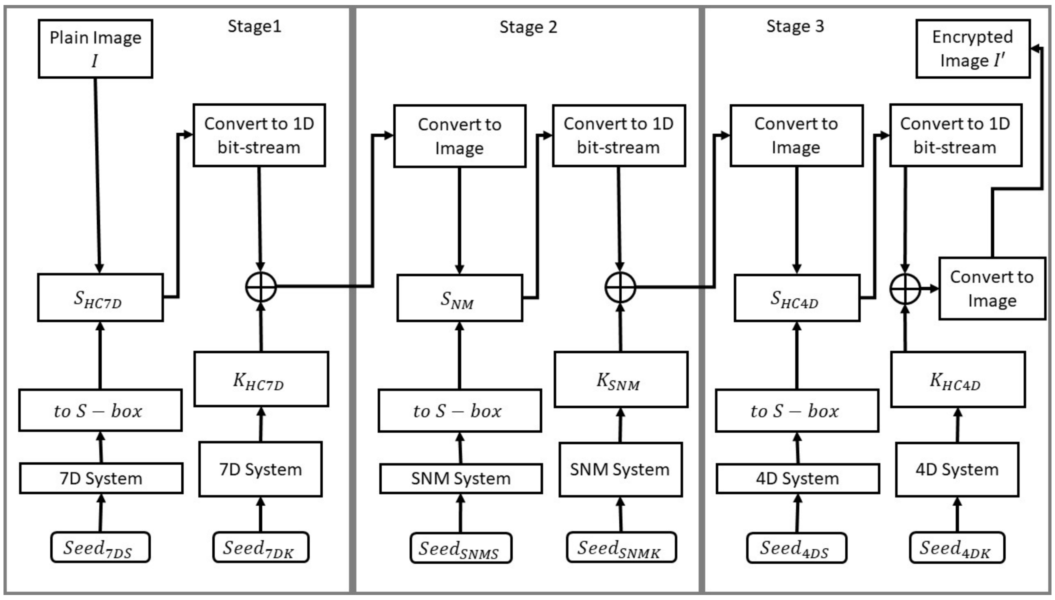

Figure 6. Flow chart of the proposed three-stage encryption process.

3.2. The Decryption Process

The following sequence of steps outlines the proposed three-stage decryption process. They are in a reverse order to those applied in the encryption process.

1. Beginning with the three-stage encrypted image $I' = I_{32}$ of length M and width N.
2. Decryption stage 3: The 4D hyperchaotic system decryption key and inverse S-box.
   (a) The pixel values of the encrypted image I_{32} are transformed into a bitstream d_{32}.
   (b) The encrypted data bits d_{32} are XORed with the decryption key k_{HC4D}.

$$d_{31} = d_{32} \oplus k_{HC4D}. \tag{11}$$

(c) The resulting encrypted data bits d_{31} are converted into an image I_{31}.
(d) A reverse replacement process is applied to image I_{31}, employing S^{-1}_{HC4D} and resulting in image I_{22}

$$I_{22} = S^{-1}_{HC4D}(I_{31}). \tag{12}$$

3. Decryption stage 2: The single neuron model decryption key and inverse S-box.
   (a) The pixel values of the encrypted image I_{22} are transformed into a bitstream d_{22}.
   (b) The encrypted data bits d_{22} are XORed with the decryption key k_{SNM}.

$$d_{21} = d_{22} \oplus k_{SNM}. \tag{13}$$

   (c) The resulting encrypted data bits d_{21} are converted into an image I_{21}.
   (d) A reverse replacement process is applied to the image I_{21}, employing S^{-1}_{SNM} and resulting in image I_{12}.

$$I_{12} = S^{-1}_{SNM}(I_{21}). \tag{14}$$

4. Decryption stage 1: The 7D hyperchaotic system decryption key and inverse S-box.
   (a) The pixel values of the encrypted image I_{12} are transformed into a bitstream d_{12}.
   (b) The encrypted data bits d_{12} are XORed with the decryption key k_{HC7D}.

$$d_{11} = d_{12} \oplus k_{HC7D}. \tag{15}$$

   (c) The resulting encrypted data bits d_{11} are converted into an image I_{11}.
   (d) A reverse replacement process is applied to the image I_{11}, employing S^{-1}_{HC7D} and resulting in a plain image I.

$$I = S^{-1}_{HC7D}(I_{11}). \tag{16}$$

A flow chart illustrative of the proposed three-stage decryption process is provided in Figure 7.

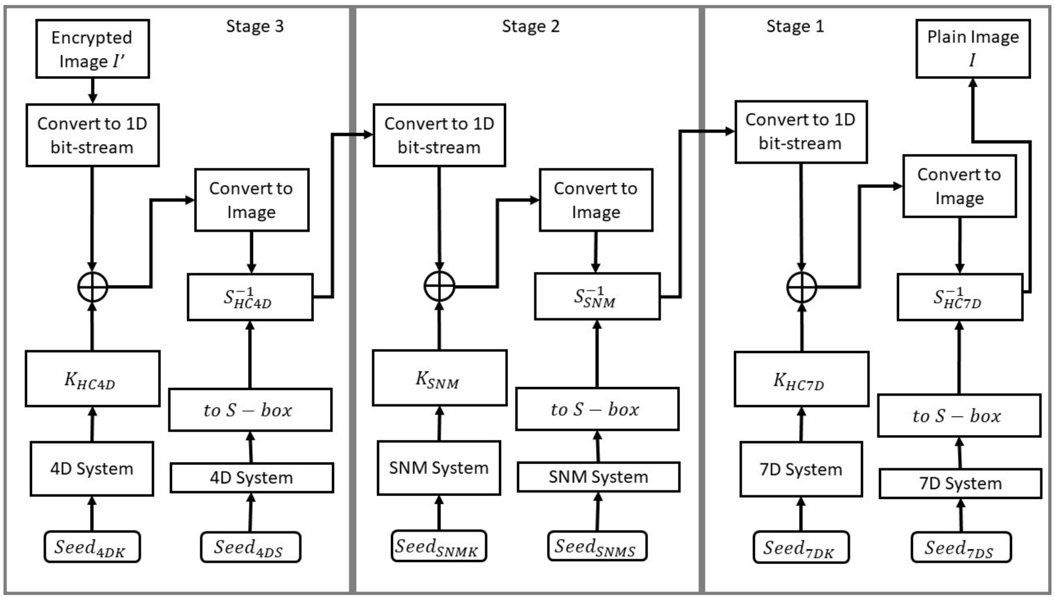

Figure 7. Flow chart of the proposed three-stage decryption process.

3.3. Utilized Algorithms

Algorithm 1 describes the generation of an S-box given a pseudo-random bitstream generated using one of the three PRNGs proposed earlier in Section 2. As discussed in Section 2.4, by treating the evaluation values of the S-box as part of the key space, Algorithm 1 attempts to achieve a certain set of provided values for S-box evaluations. The approach towards that is to generate an agreed upon number of S-boxes (which is a part of the key space as well), then each S-box is evaluated separately and the chosen S-box is the one with performance evaluation values closer to the target values. Accordingly, it may come naturally to always provide optimal S-box evaluation values for every attempt at S-box generation. Nevertheless, to fulfill the need to complicate any cryptanalysis efforts, other sub-optimal values may be provided, resulting in the generation of different S-boxes. Such a decision would not affect the overall encryption process much as each generated S-box is only one component out of many stages. Therefore, the performance evaluation of the encryption process is based on the integration of all the components in all three stages of the proposed encryption framework. Algorithm 2 elaborates on the procedure for generating a PRNG bitstream given the solution of a chaotic system.

Algorithm 1 Generate an S-box given a bitstream b_{PRNG}, the number of S-box trials n, target performance evaluation values $M = \{NL, SAC, BIC, LAP, DAP\}$ and a bitstream b_{PRNG} (an adaptation from that proposed in [12])

```
1. $S_{bits} = Partittion(b_{PRNG}, 2048)$
2. $Sbox_{res} = []$
3. $M_{res} = M$
4. For each $S_i \in S_{bits}$:
   (a) $Z_i = ToDecimal(Partition(S_i, 8))$
   (b) $L_i = [0 - 255]$
   (c) For each $U_j \in Z_i$:
       i.   $Loc_j = U_j \% Length(L_i)$
       ii.  $Append(L_i[Loc_j], Sbox_i)$
       iii. $Delete(L_i[Loc_j], L_i)$
   (d) $M_i = \{NL(Sbox_i), SAC(Sbox_i), BIC(Sbox_i), LAP(Sbox_i), DAP(Sbox_i)\}$
   (e) If $|M_i - M| < M_{res}$:
       i.  $M_{res} = |M_i - M|$
       ii. $Sbox_{res} = Sbox_i$
5. Return $Sbox_{res}$
```

Algorithm 2 Generate a PRNG bitstream given a chaotic system S of k dimensions and the number of needed bits n (first proposed in [12])

```
1. Solve $S$ for the size of $\frac{n}{k} + 1$ and the sufficient seeds producing the list of lists
   $\{L_1, L_2, ..., L_k\}$ where $L_i$ is the solution for dimension $i$
2. Convert the list of lists into a 1D list as follows:

   $$L = \{L_1[1], L_2[1], ..., L_k[1], L_1[2], L_2[2], ..., L_k[2], ...\}$$

3. Drop the last $|L| - n$ elements from $L$
4. $L_{bits}[i] = \begin{cases} 1, & \text{if } L[i] > Median(L) \\ 0, & \text{otherwise} \end{cases}$
```

4. Numerical Results and Performance Evaluation

The performance of the proposed image encryption framework is provided in this section. A number of common performance evaluation metrics from the literature are utilized in this work [2,7,12]. Their mathematical expressions are provided in Table 4. The tests carried out aim to gauge the security, robustness and efficiency of the proposed framework in eradicating any identifiable information from the output encrypted images, such that they are completely asymmetric to their plaintext versions. The proposed framework is implemented on a machine running macOS Catalina v.10.15.7 with a 2.9 GHz 6-Core Intel® Core™ i9 and 32 GB of 2400 MHz DDR4 RAM. The software of choice is Wolfram Mathematica® v.13.2. Common images found in the state-of-the-art are also utilized in this work to allow for a comparative analysis. All images are 256 pixels in length and 256 pixels in width, unless stated otherwise.

Table 4. Performance evaluation metrics and their mathematical expressions.

Metric	Mathematical Expression
MSE	$$MSE = \frac{\sum_{i=0}^{M-1}\sum_{j=0}^{N-1}(I_{(i,j)} - I'_{(i,j)})^2}{M \times N}, \quad (17)$$ where I and I' are 2 images of dimensions $M \times N$.
PSNR	$$PSNR = 10\log\left(\frac{I_{max}^2}{MSE}\right), \quad (18)$$ where $I_{max} = 255$.
MAE	$$MAE = \frac{\sum_{i=0}^{M-1}\sum_{j=0}^{N-1}\lvert I_{(i,j)} - I'_{(i,j)}\rvert}{M \times N}. \quad (19)$$
Entropy	$$H(m) = \sum_{i=1}^{M} p(m_i)\log_2\frac{1}{p(m_i)}, \quad (20)$$ where $p(m_i)$ is the probability of occurrence of symbol m, while M is the total number of bits for each symbol.
DFT	$$F(k,l) = \sum_{i=0}^{N-1}\sum_{j=0}^{N-1} f(i,j)e^{-i2\pi(\frac{ki}{N}+\frac{li}{N})}, \quad (21)$$ $f(a,b)$ is the spatial domain representation of the image, where the exponential term is the basis function corresponding to each point $F(k,l)$ in the Fourier space.
CC	$$\rho(x,y) = \frac{cov(x,y)}{\sqrt{\sigma(x)}\sqrt{\sigma(y)}}, \quad (22)$$ $$\text{where, } cov(x,y) = \frac{1}{N}\sum_{i=1}^{N}(x_i - \mu(x))(y_i - \mu(y)), \quad (23)$$ $$\sigma(x) = \frac{1}{N}\sum_{i=1}^{N}(x_i - \mu(x))^2, \text{ and } \mu(x) = \frac{1}{N}\sum_{i=1}^{N}(x_i). \quad (24)$$

Table 4. *Cont.*

Metric	**Mathematical Expression**
NPCR	$NPCR = \frac{\sum_{x=1}^{M} \sum_{y=1}^{N} D(x,y)}{M \times N} \times 100,$ (25) where, $D(x,y) = \begin{cases} 0 & I(x,y) = I'(x,y) \\ 1 & Otherwise \end{cases} \Bigg\vert x \in [1, M] \;\&\; y \in [1, N].$ (26)
UACI	$UACI = \frac{1}{M \times N} \sum_{x=1}^{M} \sum_{y=1}^{N} \frac{\lvert I(x,y) - I'(x,y) \rvert}{255} \times 100.$ (27)

4.1. Visual and Visual-Statistical Analyses

The first measure employed for testing the output encrypted images is an examination through the human visual system (HVS). It is clear from Figures 8–13 that no relation whatsoever can be observed between the plain images and their encrypted versions (i.e., complete asymmetry is achieved). The same can be noticed for their respective histograms. The histograms of the encrypted images depict a rather uniform distribution of values, which characterizes excellent encryption.

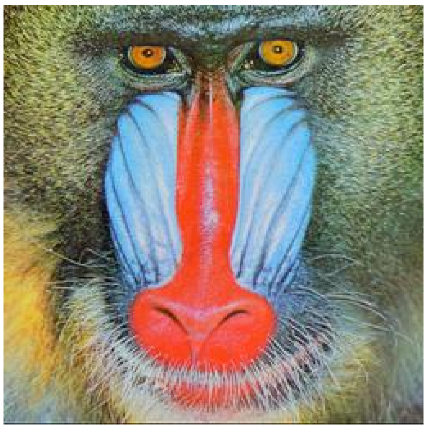
(**a**) Plain image.

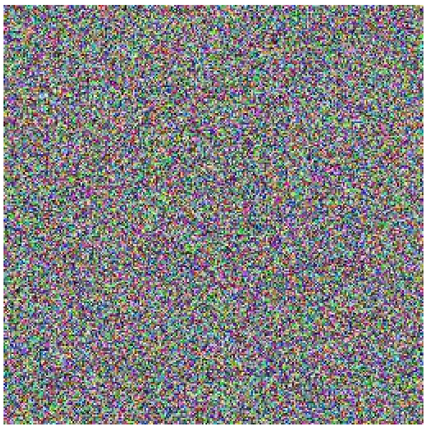
(**b**) Encrypted image.

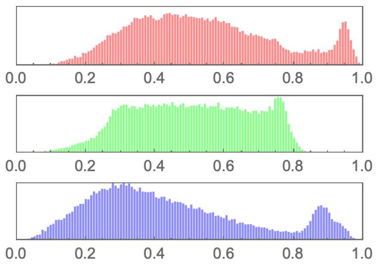

(**c**) Plain image histogram.

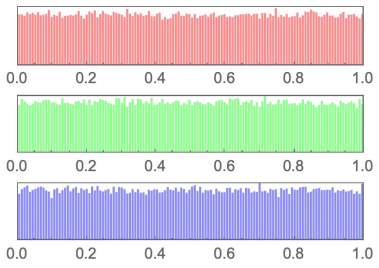

(**d**) Encrypted image histogram.

Figure 8. Mandrill image and RGB-separated histogram comparison of the plain and encrypted versions.

(**a**) Plain image.

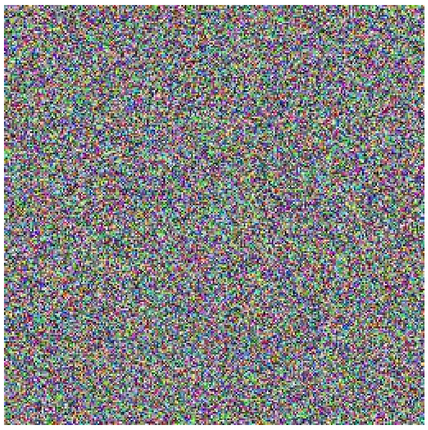
(**b**) Encrypted image.

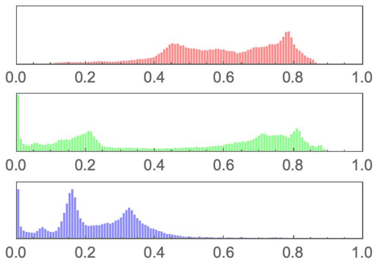

(**c**) Plain image histogram.

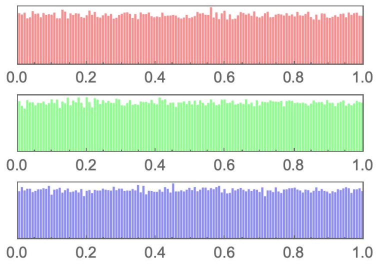

(**d**) Encrypted image histogram.

Figure 9. Peppers image and RGB-separated histogram comparison of the plain and encrypted versions.

(**a**) Plain image.

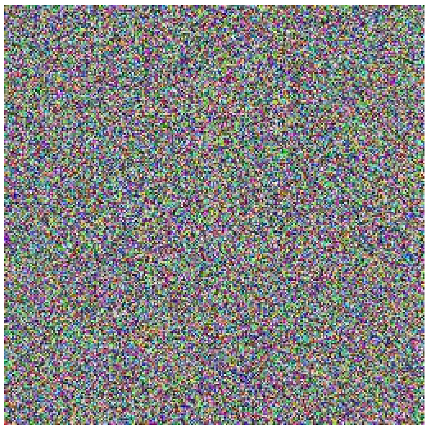
(**b**) Encrypted image.

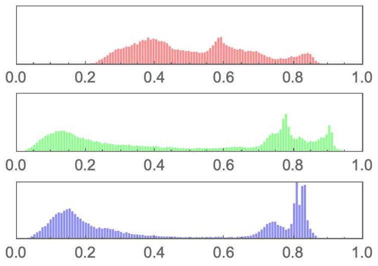

(**c**) Plain image histogram.

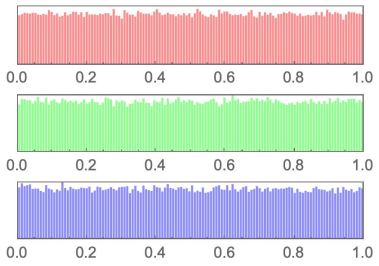

(**d**) Encrypted image histogram.

Figure 10. Sailboat image and RGB-separated histogram comparison of the plain and encrypted versions.

(**a**) Plain image.

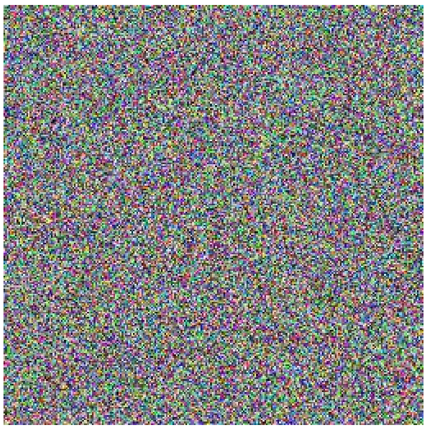
(**b**) Encrypted image.

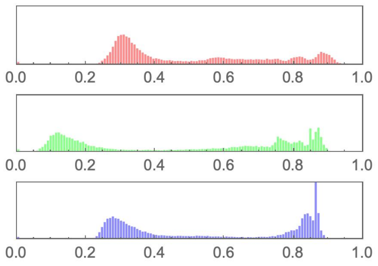

(**c**) Plain image histogram.

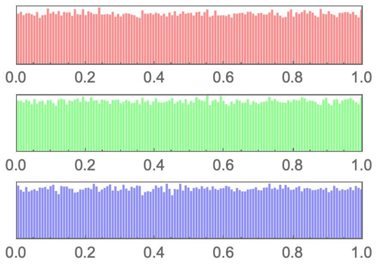

(**d**) Encrypted image histogram.

Figure 11. Tree image and RGB-separated histogram comparison of the plain and encrypted versions.

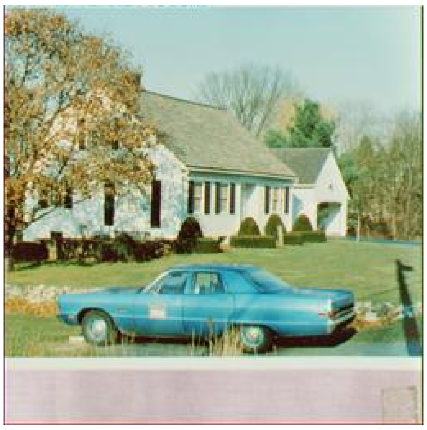
(**a**) Plain image.

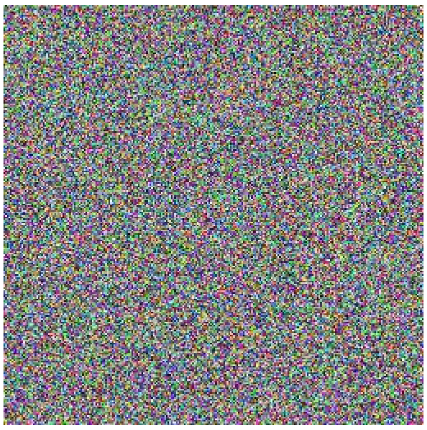
(**b**) Encrypted image.

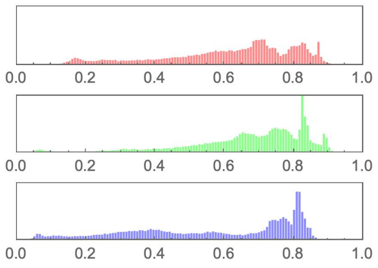

(**c**) Plain image histogram.

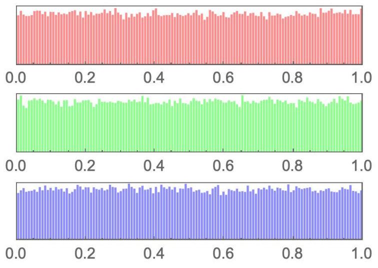

(**d**) Encrypted image histogram.

Figure 12. House2 image and RGB-separated histogram comparison of the plain and encrypted versions.

(**a**) Plain image.

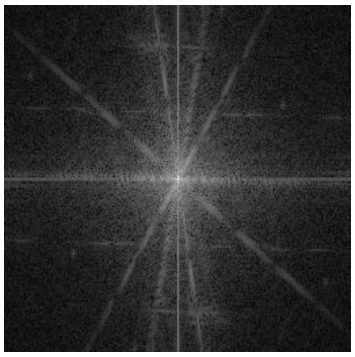
(**b**) Plain image DFT.

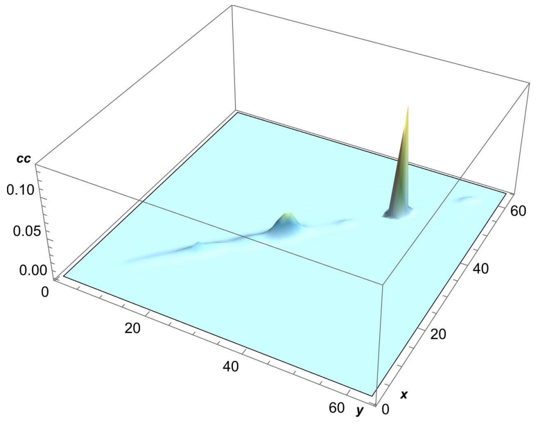

(**c**) Plain image pixel cross-correlation.

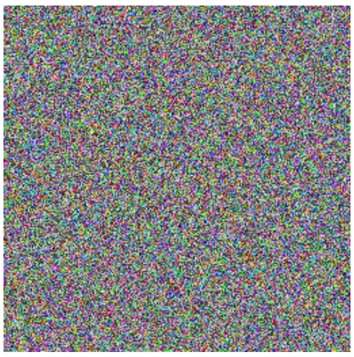
(**d**) Encrypted image.

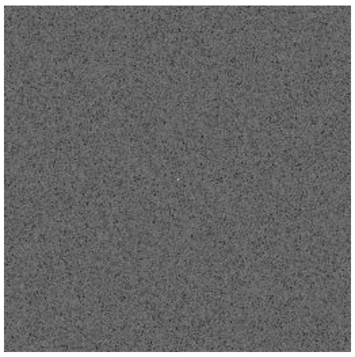
(**e**) Encrypted image DFT.

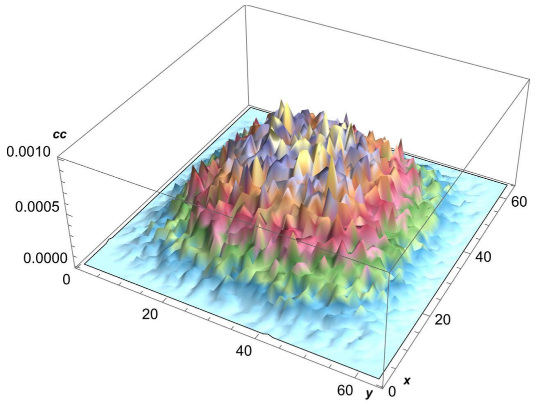

(**f**) Encrypted image pixel cross-correlation.

Figure 13. House image, its DCT, and 3D plot of its pixel cross-correlation matrix pre- and post-encryption.

4.2. Statistical Analyses

The statistical analysis starts with the computation of the mean squared error (MSE), the peak signal-to-noise ratio (PSNR) and the maximum absolute error (MAE) between input plain images and output encrypted images. These are quantitative metrics that measure the degree of change between two images and are very common in the literature on image encryption. The computed values are reported in Tables 5–7, respectively. It is clear from each of the tables that the computed values for the proposed image encryption algorithm are comparable or superior to the state-of-the-art, with high MSE and MAE values and thus low PSNR values, indicating excellent scrambling and randomization performance of the proposed image encryption framework.

As for Shannon's information entropy, Table 8 displays the computed values for various encrypted images and compares those values with the state-of-the-art. Excellent entropy performance of 7.999 is showcased for the proposed image encryption framework, being superior or comparable to counterpart algorithms.

The pixel cross-correlation coefficient ρ is a measure of the linear dependency between neighboring pixel values in an image. It quantifies how well the encryption process has scrambled the pixels and eliminated any spatial relationships. For a well-encrypted image, ρ should have a value close to 0, indicating little or no correlation between adjacent pixel values. Table 9 provides the ρ values for various images, each computed in three directions (horizontal, vertical and diagonal). While the plain images have ρ values close to 1, their encrypted versions have ρ values close to 0. A visual illustration of this metric is provided as a set of 2D plots in Figure 14 for the House image, as well as in Figures 15–17, respectively, for each of its RGB channels, while sub-figures (c) and (f) of Figure 13 provide 3D plots of the same metric for the House image. It is clear that the plots of encrypted images exhibit a uniform distribution of values, unlike those of their plain versions. Tables 10 and 11 display a comparison of ρ with the state-of-the-art, utilizing the Lena image and each of its RGB channels, respectively. The computed ρ values are shown to be near 0, as is the case in the state-of-the-art, in each of the tables.

Another interesting manner of examining the pixel cross-correlation among pixels would be to do so in the Fourier domain by generating the discrete Fourier transform (DFT) of the plain and encrypted House images, as shown in sub-figures (b) and (e) of Figure 13 and visually examining them. The presence of a bright star-like shape at the center of the DFT plain image is characteristic of a normal plain image which has pixels depicting edges and corners. This is unlike the DFT of the encrypted image, which lacks any identifying visual characteristics.

Since randomness is an integral measure of any image encryption algorithm, an objective quantitative measure of it should be utilized. This is best carried out through a National Institute of Standards and Technology (NIST) SP 800 analysis [37]. In brief, a NIST analysis tests a bitstream for a number of characteristics, including its randomness, quantifies its randomness and detects structural weaknesses. Such an analysis provides empirical evidence of the suitability of a PRNG's use in cryptography applications. Table 12 presents the results of a NIST analysis carried out on a bitstream depicting the data of an encrypted Girl image. All NIST tests are successfully passed, with scored p-values greater than 0.01.

Table 5. MSE values for various images, for the proposed framework and the state-of-the-art.

Image	Proposed	[7]	[13]	[38]	[15]	[6]	[19]	[12]
Lena	8890.05	9112.1	8926.96	10,869.73	4859.03	8888.88	N/A	8912.4
Mandrill	8345.25	8573.38	8290.84	10,930.33	6399.05	8295.21	N/A	8320.41
Peppers	10,074.0	10,298.7	10,045.1	N/A	7274.44	10,092.3	N/A	10,065.4
House	8361.44	8427.04	8351.64	N/A	N/A	N/A	N/A	8395.53
House2	9190.27	9374.65	N/A	N/A	N/A	N/A	N/A	9142.54
Girl	12,152.8	12,450.9	N/A	N/A	N/A	N/A	N/A	12,104.2
Sailboat	10,063.3	N/A	N/A	N/A	N/A	N/A	N/A	10,071.9
Tree	9931.63	N/A	N/A	N/A	N/A	N/A	N/A	9873.24
Average	9626.09	9706.13	8903.64	10,900	6177.51	9092.13	N/A	9610.65

Table 6. PSNR values for various images, for the proposed framework and the state-of-the-art.

Image	Proposed	[7]	[13]	[38]	[15]	[6]	[19]	[12]
Lena	8.64176	8.53462	8.6237	7.7677	11.3	8.64233	8.5674	8.63086
Mandrill	8.91641	8.79929	8.9448	7.7447	10.10	8.94253	10.0322	8.92936
Peppers	8.09877	8.00296	8.11128	N/A	9.55	N/A	N/A	8.10248
House	8.90799	8.87405	8.91309	N/A	N/A	N/A	N/A	8.89032
House2	8.49752	8.41125	N/A	N/A	N/A	N/A	N/A	8.52013
Girl	7.28403	7.17879	N/A	N/A	N/A	N/A	N/A	7.30144
Sailboat	8.10339	N/A	N/A	N/A	N/A	N/A	N/A	8.0997
Tree	8.1606	N/A	N/A	N/A	N/A	N/A	N/A	8.18621
Average	8.32631	8.30016	8.64822	7.7562	10.3167	8.79243	9.2998	8.33256

Table 7. MAE values for various images, for the proposed framework and the state-of-the-art.

Image	Proposed	[7]	[6]	[38]	[39]	[19]	[12]
Lena	77.409	78.3564	77.3752	87	77.35	77.96	77.4877
Peppers	82.0156	82.3273	81.7740	N/A	74.71	N/A	81.9832
Mandrill	75.3335	81.913	75.1659	92	73.91	67.85	75.1632
House	75.3132	N/A	N/A	N/A	N/A	N/A	75.4983
House2	78.5675	N/A	N/A	N/A	N/A	N/A	78.3327
Girl	90.1646	N/A	N/A	N/A	N/A	N/A	89.9807
Sailboat	82.0101	N/A	N/A	N/A	N/A	N/A	82.1003
Tree	81.4948	N/A	N/A	N/A	N/A	N/A	81.1623
Average	80.9993	80.8656	78.105	89.5	75.3233	72.905	80.2136

Table 8. Entropy values for various images, for the proposed framework and the state-of-the-art.

Image	Proposed	[7]	[13]	[38]	[40]	[15]	[6]	[19]	[12]
Lena	7.999	7.9856	7.999	7.999	7.997	7.996	7.997	7.9972	7.99887
Mandrill	7.999	7.9905	7.999	7.999	7.999	N/A	7.996	7.9969	7.99866
Peppers	7.999	7.9951	7.999	7.9991	N/A	7.997	7.9969	N/A	7.99834
House	7.999	7.9577	7.999	N/A	N/A	N/A	N/A	N/A	7.99729
House2	7.999	7.9847	N/A	N/A	N/A	N/A	N/A	N/A	7.99848
Girl	7.999	7.9789	N/A	N/A	N/A	N/A	N/A	N/A	7.99477
Sailboat	7.999	N/A	N/A	N/A	N/A	N/A	N/A	N/A	7.99875
Tree	7.999	N/A	N/A	N/A	N/A	N/A	N/A	N/A	7.99713
Average	7.999	7.98208	7.999	7.999	7.99903	7.9965	7.99663	7.99705	7.99711

Table 9. Correlation coefficient values for various plain and encrypted images.

	Plain Image			Encrypted Image		
	Correlation Coefficient			Correlation Coefficient		
Image	**Horizontal**	**Diagonal**	**Vertical**	**Horizontal**	**Diagonal**	**Vertical**
Lena	0.938611	0.913175	0.96833	0.00180128	−0.000991502	−0.00018608
Mandrill	0.848778	0.750624	0.79088	0.00713777	−0.00152782	0.00491305
Peppers	0.959422	0.930426	0.966795	0.00301689	0.00419115	−0.00012237
House	0.978232	0.936044	0.952926	−0.00147997	−0.00286442	−0.0015624
House2	0.907075	0.850782	0.923091	0.000841531	−0.00214171	−0.00626431
Girl	0.974013	0.951471	0.965671	0.000841531	−0.00214171	−0.00626431
Sailboat	0.952381	0.0.919872	0.950138	0.00608092	0.00279574	0.00170383
Tree	0.968153	0.929967	0.94515	−0.00226616	0.00137505	0.00332063

Table 10. Correlation coefficient values comparison with the state-of-the-art, for an encrypted Lena image.

Algorithm	Horizontal	Diagonal	Vertical
Proposed	0.00180128	−0.000991502	−0.000186079
[6]	0.002287	−0.00132	−0.00160
[7]	0.003265	−0.00413	0.002451
[12]	0.0064113	−0.0015143	0.000568333
[17]	0.00144	−0.00151	0.00795
[19]	−0.0061	−0.0018	0.0067
[22]	0.000199	0.003705	−0.000924
[38]	0.0054	0.0054	0.0016

Table 11. Color channel separated correlation coefficient value comparison with the state-of-the-art, for the Lena image.

Channel	Direction	Plain Image	Encrypted Image	[23]	[24]	[25]	[6]
Red	Horizontal	0.952474	0.00266725	0.001365	0.0021	0.9568	−0.00364
	Diagonal	0.928029	0.00564219	0.000232	−0.0026	0.0075	0.00016
	Vertical	0.975913	−0.0008351	0.004776	0.0018	−0.0376	0.000697
Green	Horizontal	0.935628	0.00307568	0.003294	−0.0006	0.0020	0.000118
	Diagonal	0.910534	−0.0020740	0.004807	0.0001	−0.0046	0.00177
	Vertical	0.966647	−0.0011823	−0.000579	0.0004	−0.0013	−0.0011
Blue	Horizontal	0.917439	−0.00046821	0.002060	−0.005	0.0071	−0.00164
	Diagonal	0.888482	−0.0025489	−0.004043	−0.0104	−0.0009	−0.00523
	Vertical	0.947961	0.0053944	0.000194	0.001	−0.0423	0.006041

Table 12. NIST analysis on Girl encrypted image.

Test Name	Value	Remarks
Frequency	0.425242	Success
Block Frequency	0.276783	Success
Run	0.714157	Success
Longest run of ones	0.932530	Success
Rank	0.138292	Success
Spectral FFT	0.846825	Success
Non overlapping	0.613084	Success
Overlapping	0.449023	Success
Universal	0.687511	Success
Linear complexity	0.241374	Success
Serial	0.850353	Success
Approximate Entropy	0.030357	Success
Cumulative sum (forward)	0.503876	Success
Cumulative sum (reverse)	0.783156	Success

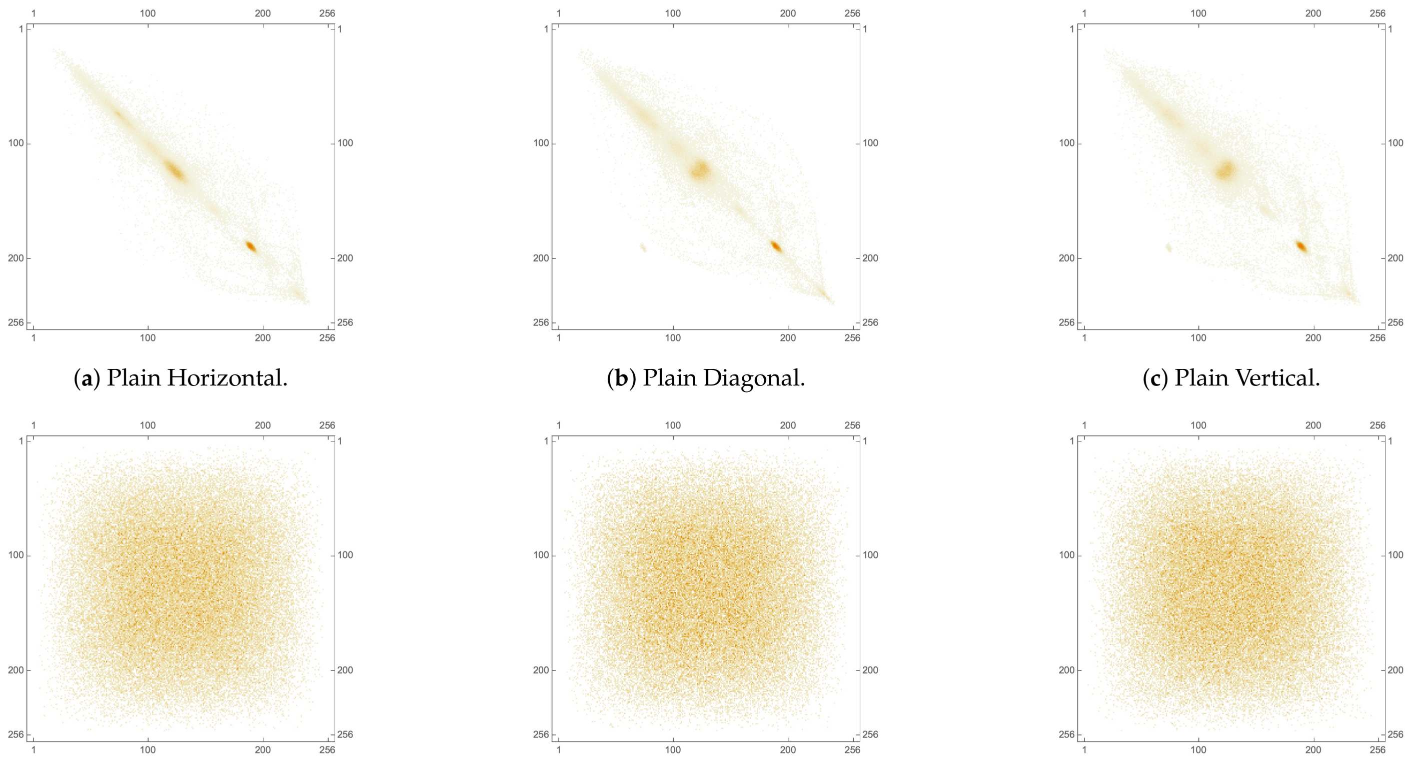
(**a**) Plain Horizontal. (**b**) Plain Diagonal. (**c**) Plain Vertical.

(**d**) Encrypted Horizontal. (**e**) Encrypted Diagonal. (**f**) Encrypted Vertical.

Figure 14. Two-dimensional plot of pixel cross-correlation matrices of the House image pre- and post-encryption.

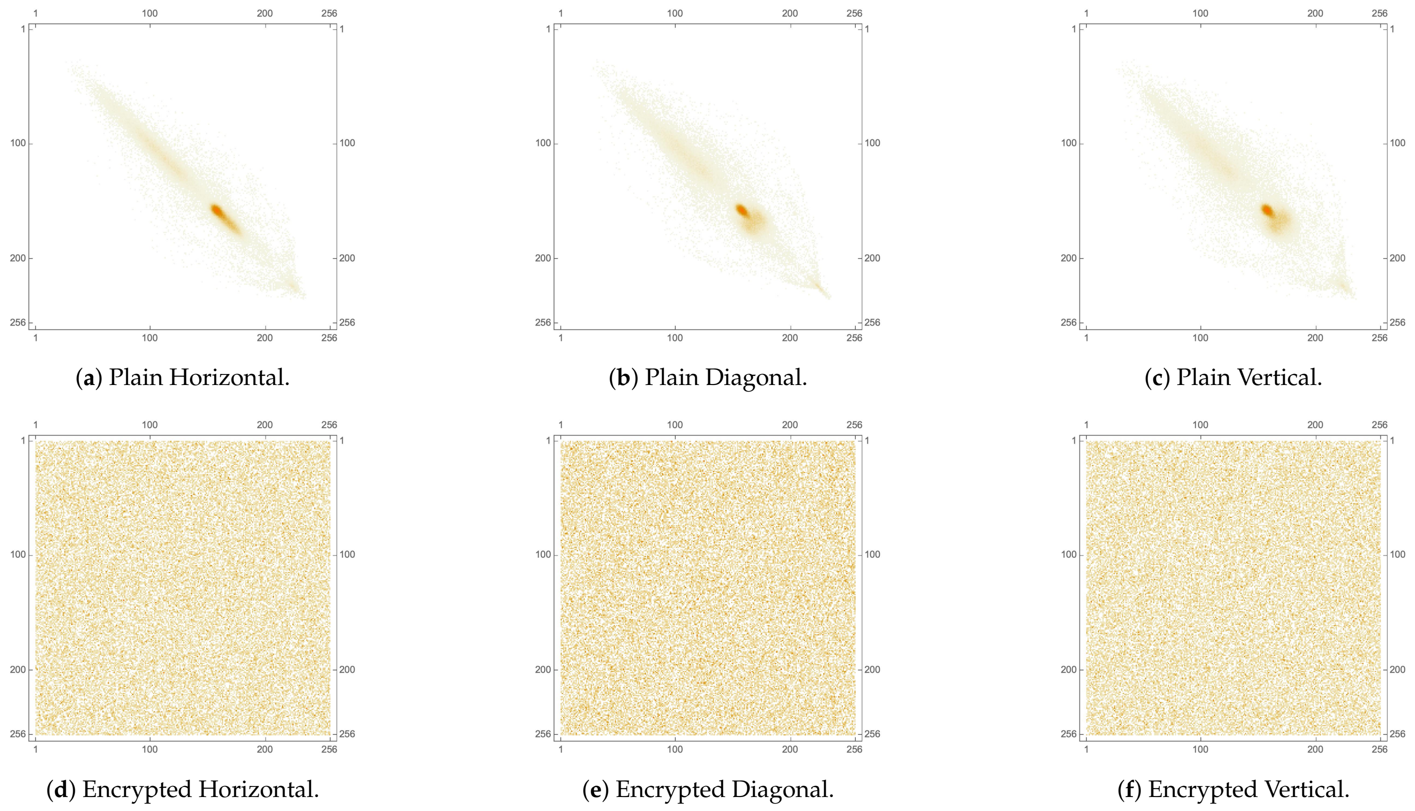

(**a**) Plain Horizontal. (**b**) Plain Diagonal. (**c**) Plain Vertical.

(**d**) Encrypted Horizontal. (**e**) Encrypted Diagonal. (**f**) Encrypted Vertical.

Figure 15. Two-dimensional plot of pixel cross-correlation matrices of the **red** channel of the House image pre- and post-encryption.

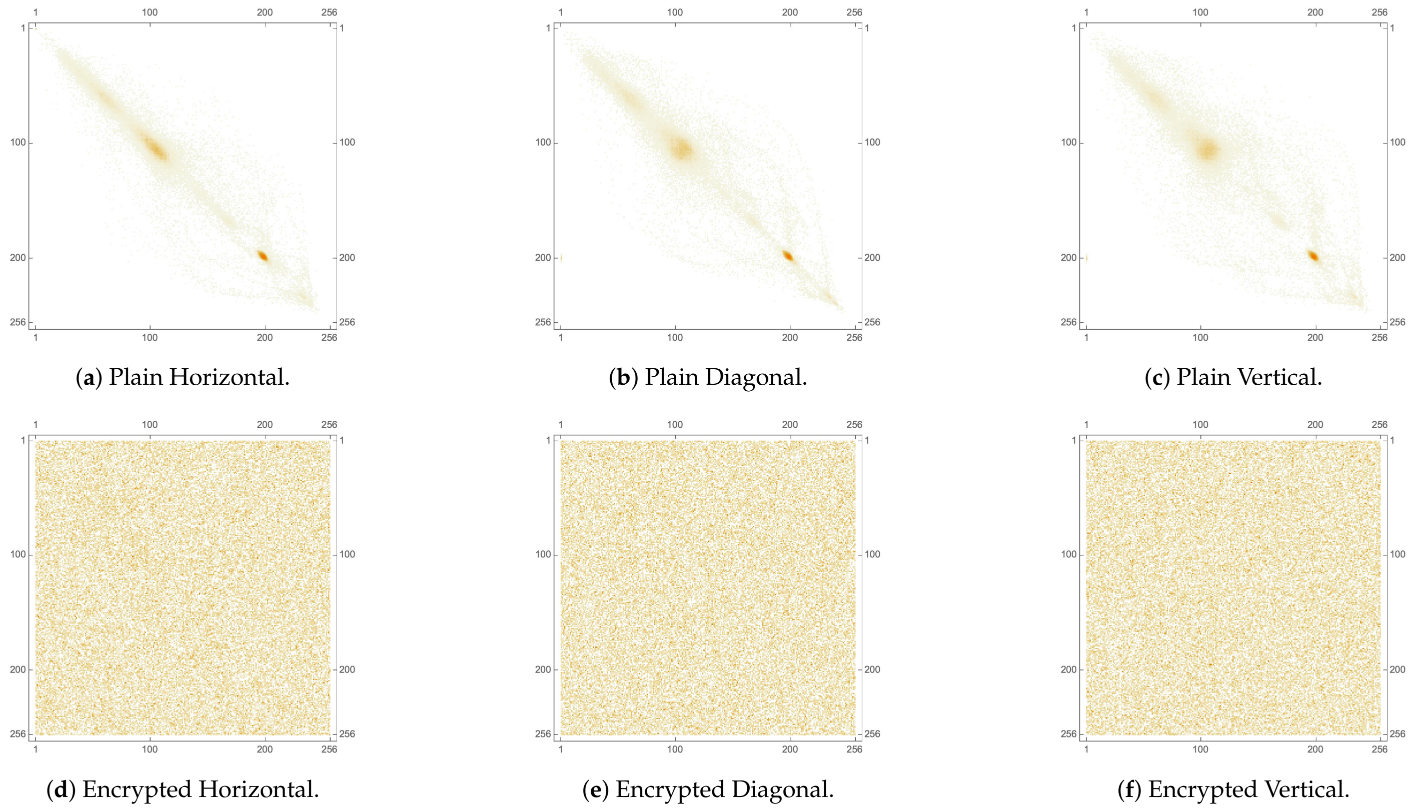

(**a**) Plain Horizontal. (**b**) Plain Diagonal. (**c**) Plain Vertical.

(**d**) Encrypted Horizontal. (**e**) Encrypted Diagonal. (**f**) Encrypted Vertical.

Figure 16. Two-dimensional plot of pixel cross-correlation matrices of the **green** channel of the House image pre- and post-encryption.

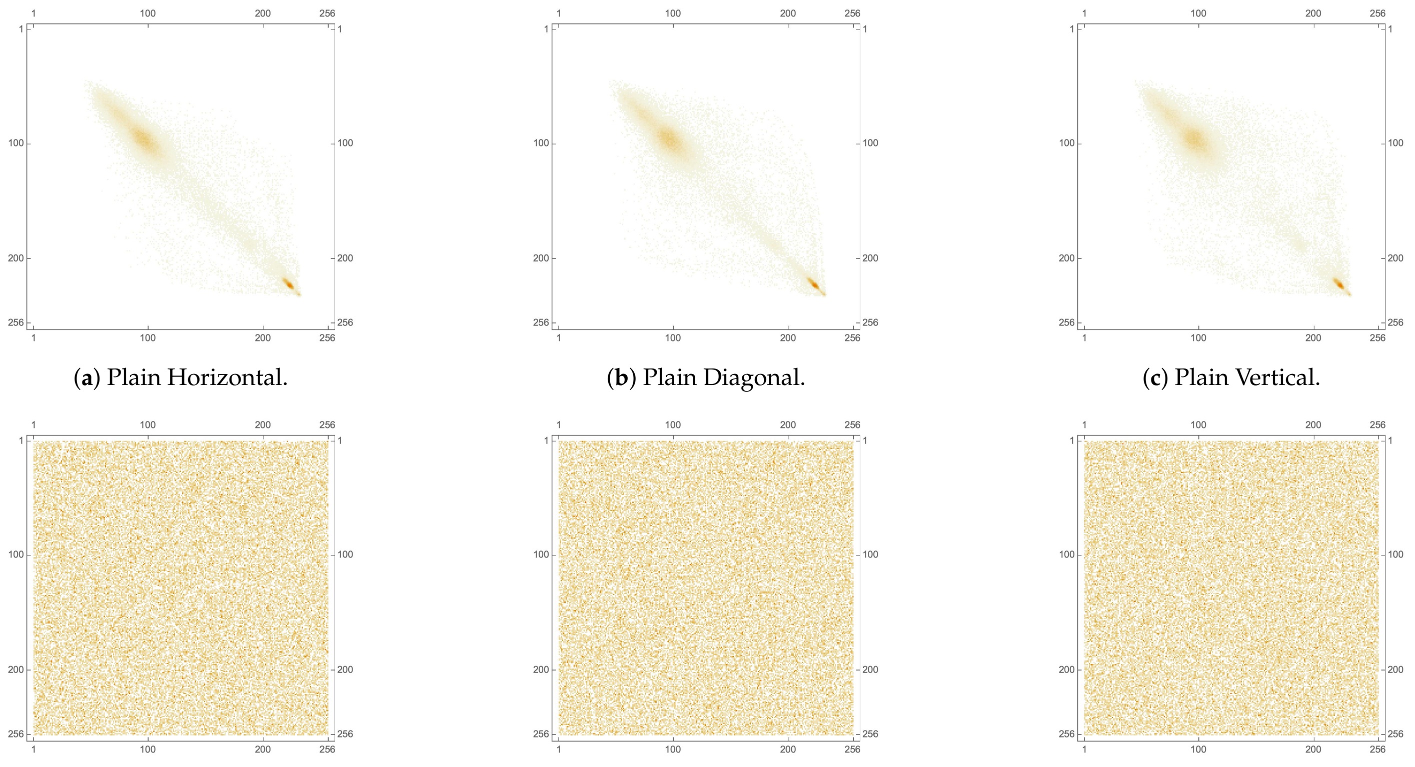

(**a**) Plain Horizontal. (**b**) Plain Diagonal. (**c**) Plain Vertical.

(**d**) Encrypted Horizontal. (**e**) Encrypted Diagonal. (**f**) Encrypted Vertical.

Figure 17. Two-dimensional plot of pixel cross-correlation matrices of the **blue** channel of the House image pre- and post-encryption.

4.3. Differential Attack Analysis

A differential attack analysis is a type of cryptanalytic attack on encryption algorithms where an attacker analyzes the effect of specific changes in the input plaintext on the output ciphertext. For example, the change of a single bit in the input plain image. By analyzing these differences, the attacker may be able to deduce information about the key or algorithm used. Two tests are commonly employed in the literature for such an analysis: The number of pixel change ratios (NPCR) for pixel-by-pixel comparison and the unified averaged change intensity (UACI) for the evaluation of the mean average difference [41] have ideal values for well-encrypted images of 100% and 33.33%, respectively. The mathematical expressions corresponding to each of those metrics are provided in Table 4. The computed NPCR and UACI values for various images are displayed in Table 13, with achieved average values of 99.6186% and 31.4857%, respectively, reflecting excellent performance. Table 14 compares the computed values with the state-of-the-art for the RGB channels of various images. As expected, a comparable performance is achieved. Moreover, Table 15, displays another comparison with counterpart algorithms for the Lena image. Once again, a comparable performance is achieved.

Table 13. NPCR and UACI values of various images.

Metric	Image	Result
NPCR	Lena	99.6114
	Peppers	99.6267
	Mandrill	99.6094
	House	99.6165
	House2	99.6318
	Girl	99.6287
	Sailboat	99.6318
	Tree	99.5926
	Average	99.6186

Table 13. *Cont.*

Metric	Image	Result
UACI	Lena	30.3565
	Peppers	32.163
	Mandrill	29.5425
	House	29.5346
	House2	30.8108
	Girl	35.3587
	Sailboat	32.1608
	Tree	31.9587
	Average	31.4857

Table 14. NPCR and UACI values comparison with the state-of-the-art for various images.

Metric	Image	Color Channel	Proposed	[6]	[42]	[12]
NPCR	Lena	Red	99.6231	99.6109	99.6355	99.5712
		Green	99.614	99.6109	99.6256	99.5758
		Blue	99.5972	99.6375	99.6159	99.6094
	Peppers	Red	99.6002	99.6032	99.6307	99.6338
		Green	99.6429	99.6032	99.6250	99.6338
		Blue	99.6368	99.3750	99.6213	99.6628
	Mandrill	Red	99.5819	99.5880	99.6102	99.5911
		Green	99.6292	99.5880	99.6134	99.5865
		Blue	99.617	99.5880	99.6057	99.6292
UACI	Lena	Red	32.8621	33.4158	33.4657	33.1056
		Green	30.6466	30.3902	33.4552	30.5178
		Blue	27.5607	33.2420	33.4550	27.5385
	Peppers	Red	28.9367	33.3459	33.4832	28.8353
		Green	33.8071	33.4702	33.4904	33.8409
		Blue	33.7452	33.4357	33.4619	33.7746
	Mandrill	Red	29.7236	33.4273	33.5002	29.5137
		Green	28.0515	33.4635	33.4711	28.0464
		Blue	30.8524	33.7951	33.4951	30.8671

Table 15. NPCR and UACI values comparison of the Lena image with the state-of-the-art.

Scheme	NPCR	UACI
Proposed	99.6114	30.3565
[2]	99.625	30.5681
[6]	99.63	30.3432
[12]	99.5855	30.3873
[17]	99.6246	30.5681
[19]	99.61	33.516
[38]	99.52	26.793
[43]	99.63	33.48
[44]	99.61	33.434

4.4. Key Space Analysis

It is of vital importance to carry out a key space analysis of any image encryption technique. Such an analysis quantifies how much information (in bits) is required to specify an encryption key. The more bits needed, the larger the key space. Consequently, a large key space makes brute-force attacks infeasible. The larger the number of possible keys, the greater the resources and time required to try every key. This helps ensure encryption is secure against brute-force cracking. In the proposed image encryption framework, the attained key space is vast, mainly due to the utilization of the hyperchaotic maps. The 4D hyperchaotic map employs four initial values and seven constants; the 7D hyperchaotic map employs seven initial conditions and 10 constants; and the SNM employs a total of five variables only. For each of the three S-boxes, five specific values for the metrics are chosen. This gives a total of $4 + 7 + 7 + 10 + 5 + 3 \times 5 = 48$ variables in the computation of the key space. The computer and software package used to implement the proposed image encryption framework have a machine precision of 10^{-16}. Ultimately, this gives a key space of $10^{48\times16} = 10^{768} \approx 2^{2551}$. This computed value far surpasses the threshold suggested earlier in the literature [45], of 2^{100}, for successful resistance to brute-force attacks. A comparative analysis is carried out with the state-of-the-art in Table 16, showcasing the superior key space of the proposed image encryption framework.

Table 16. A comparison of key space values with the state-of-the-art.

Algorithm	Key Space
Proposed	2^{2551}
[2]	2^{478}
[7]	2^{372}
[12]	2^{1658}
[17]	2^{554}
[19]	2^{604}
[20]	2^{312}
[21]	2^{256}
[22]	2^{187}
[26]	2^{128}
[27]	2^{219}

4.5. Histogram Dependency Tests

In this testing perspective, the histograms of the plain and encrypted images are statistically compared in order to show the lack of statistical dependence between the two. Table 17 shows the five utilized tests (Blomqvist β, Goodman–Kruskal γ, Kendall τ, Spearman ρ and Pearson r) and their mathematical expressions [46]. Table 18 demonstrates the results of applying these tests to a variety of images. As seen in the table, most of the resulting values approach 0, which shows a lack of any statistical dependency between every plain image and its encrypted version.

Table 17. Histogram dependency tests and their mathematical expressions.

Metric	Mathematical Expression
Blomqvist	$\beta = \{(X-\overline{x})(Y-\overline{y}) > 0\} - \{(X-\overline{x})(Y-\overline{y}) < 0\}. \quad (28)$
Goodman–Kruskal	$\gamma = \frac{n_c - n_d}{n_c + n_d}. \quad (29)$
Kendall	$\tau = \frac{n_c - n_d}{\frac{n(n-1)}{2}}. \quad (30)$
Spearman	$\rho = \frac{\sum(R_{ix}-\overline{R}_x)(R_{iy}-\overline{R}_y)}{\sqrt{\sum(R_{ix}-\overline{R}_x)^2\sum(R_{iy}-\overline{R}_y)^2}}. \quad (31)$
Pearson	$r = \frac{\sum(X_i-\overline{X})(Y_i-\overline{Y})}{\sqrt{\sum(X_i-\overline{X})^2\sum(Y_i-\overline{Y})^2}}. \quad (32)$

Table 18. Tests of histogram dependency for various images.

Image	Color	β (28)	γ (29)	τ (30)	ρ (31)	r (32)
Lena	Red	0.00397832	0.0313687	0.0303408	0.0434341	0.0270663
	Green	0	0.0215872	0.014269	0.0166966	0.0193475
	Blue	−0.0793976	−0.0608106	−0.0572115	−0.0818634	−0.109206
	Combined	0.0277309	−0.0199151	−0.0198071	−0.0329345	−0.0468979
Peppers	Red	−0.0316218	−0.0270098	−0.0264574	−0.036404	−0.0223967
	Green	0.0355072	0.0185307	0.0183487	0.0317549	0.0375528
	Blue	−0.00396106	−0.0164391	−0.016167	−0.0263073	−0.0482875
	Combined	0.0948802	0.0436563	0.0433807	0.0645118	0.0666087
Mandrill	Red	−0.0198078	−0.0466956	−0.0462145	−0.0686459	−0.0672317
	Green	0.0676058	0.0704028	0.0691334	0.099575	0.108835
	Blue	−0.00394524	−0.027233	−0.0269739	−0.0414617	−0.032399
	Combined	0.0316238	−0.00105387	−0.00104776	−0.00335102	−0.00619468
House	Red	−0.078125	−0.0735036	−0.0713676	−0.10807	0.129594 − 0.124939
	Green	0.0278483	0.0505291	0.0499853	0.0757827	0.100048
	Blue	−0.0558677	−0.0186177	−0.0178087	−0.0270381	−0.0762734
	Combined	−0.03125	−0.0270421	−0.0268626	−0.0384522	−0.0603119
House2	Red	−0.122785	−0.11135	−0.109577	−0.159726	−0.187521
	Green	−0.0159414	−0.00680612	−0.00674228	−0.00405984	0.0230262
	Blue	0.0560937	0.0890006	0.0876046	0.131527	0.132005
	Combined	−0.109375	−0.0772136	−0.0768099	−0.110878	−0.0822007
Girl	Red	0.0830847	0.0581335	0.0489882	0.0663806	0.0108236
	Green	0.0336761	0.0192351	0.0159392	0.0191791	0.0103639
	Blue	−0.0232813	−0.0120988	−0.00979622	−0.0113034	−0.0309034
	Combined	0.15625	0.0462478	0.0441833	0.0606254	−0.00724911
Sailboat	Red	−0.0158755	0.00608236	0.00584084	0.00894156	0.015278
	Green	−0.0994093	−0.0609726	−0.060292	−0.0933644	−0.0969401
	Blue	−0.0357981	−0.0261754	−0.025861	−0.0370723	−0.104682
	Combined	0.031754	−0.0324742	−0.0322749	−0.0539398	−0.123518
Tree	Red	−0.0239129	−0.0587334	−0.0575335	−0.0886452	−0.116216
	Green	0.00401018	0.00607749	0.00597875	0.00638248	−0.0328477
	Blue	0.0236235	0.0389318	0.0374368	0.0573412	0.0216757
	Combined	0.015625	0.00158429	0.00157335	0.00789208	−0.0243032

4.6. Execution Time Analysis

The execution time of an image encryption algorithm is an important metric, as it allows for a comparison of the efficiency and performance of different algorithms as well as an estimation of the computational resources required for software and hardware implementation. Moreover, an analysis of the execution time reveals the applicability of an algorithm for real-time image encryption applications. The software implementation of the proposed image encryption framework is carried out over Wolfram Mathematica® v.13.2. The algorithm's execution time is optimized through parallel processing over the six cores of the Intel® Core$^{\text{TM}}$ i9 processor. The full details of the computing environment are provided in the first paragraph of Section 4. Table 19 reports the attained execution times of the Lena image at various dimensions. These times result in an average encryption rate of 8.54 Mbps. Moreover, Table 20 provides a comparative analysis of the state-of-the-art algorithms. The superiority of the proposed framework is clear, with the attained encryption times being much shorter in comparison to their counterparts, irrespective of the machine specifications.

Table 19. Execution times, in terms of encryption, decryption and their combined values for the proposed framework at various image dimensions.

Image Dimensions	t_{Enc} (s)	t_{Dec} (s)	t_{Add} (s)
64×64	0.011306	0.011419	0.0227249
128×128	0.039643	0.038158	0.077801
256×256	0.167471	0.161055	0.328526
512×512	0.732927	0.751684	1.48461
1024×1024	2.99817	3.161	6.15917

Table 20. A comparison of the encryption time for various algorithms from the literature for a Lena image with dimensions 256×256.

Algorithm	t_{Enc} (s)	Machine Specifications (CPU and RAM)
Proposed	0.167471	2.9 GHz Intel® Core^{TM} i9, 32 GB
[2]	2.750966	3.4 GHz Intel® Core^{TM} i7, 8 GB
[6]	2.582389	2.9 GHz Intel® Core^{TM} i9, 32 GB
[7]	1.42545	2.9 GHz Intel® Core^{TM} i9, 32 GB
[12]	0.426243	2.9 GHz Intel® Core^{TM} i9, 32 GB
[17]	3.0019	3.4 GHz Intel® Core^{TM} i7, 8 GB
[19]	2.7236	2.7 GHz Intel® Core^{TM} i7, 8 GB
[27]	3.45	N/A
[28]	1.112	3.4 GHz Intel® Core^{TM} i3, 4 GB
[29]	1.1168	3.4 GHz Intel® Core^{TM} i7, 8 GB

4.7. S-Box Performance Analysis

The proposed S-boxes are evaluated in this section independently of the proposed framework's performance as a whole. This is because an S-box is a consistent element that is nearly always at the core of image encryption algorithms and is tasked with applying Shannon's property of confusion. In order to evaluate the ability of an S-box to cause confusion, five metrics are commonly computed [47]. These are the non-linearity (NL), linear approximation probability (LAP), differential approximation probability (DAP), bit independence criterion (BIC) and strict avalanche criterion (SAC). They are calculated for the proposed S-boxes (shown in Tables 1–3) and compared to those reported in the state-of-the-art as well as to the ideal values, in Table 21. While all three proposed S-boxes exhibit performances comparable to counterpart algorithms from the literature, it is clear that the S-boxes constructed from the hyperchaotic functions perform better than the S-box constructed from the SNM. This is an advantage of hyperchaotic functions [48]. As in [12] and as described earlier in Section 3.3, upon designing and constructing each of the proposed S-boxes, the aim is not to reach the ideal values of the metrics but rather to reach a set of target metrics that are in close proximity to the ideal ones. This was carried out so as to include this set of target values as part of the key space, expanding it by $5 \times 3 = 15$ variables and allowing it to reach a key space of 2^{2551}, as explained earlier in Section 4.4.

Table 21. Comparison of the numerical evaluation of the proposed S-boxes (displayed in Tables 1–3) among those provided in the literature.

S-box	NL	SAC	BIC	LAP	DAP
Ideal values	112	0.5	112	0.0625	0.015625
Proposed, SNM (1)	106	0.499268	104	0.09375	0.015625
Proposed, HC 4D (2)	108	0.500977	108	0.078125	0.015625
Proposed, HC 7D (3)	108	0.506592	108	0.078125	0.015625
[12] MT	108	0.503662	92	0.140625	0.015625
[12] OpenSSL	108	0.499023	112	0.0625	0.015625
[12] Intel's MKL	108	0.499268	104	0.09375	0.015625
[38]	111	0.5036	110	0.0781	0.0234
[49]	107	0.497	103.5	0.1560	0.0390
[50]	100	0.5007	104.1	0.0390	0.1250
[51] S4	112	0.5	112	0.0625	0.0156

5. Conclusions and Future Works

This work attempted to propose a novel framework for image encryption, capitalizing on the inherent characteristics of hyperchaotic functions and the simplicity of the single neuron model. Encryption was carried out over three stages, where in each stage the solution of one of the systems was numerically computed and used to generate a PRNG and construct an S-box. Next, the S-box was applied to scramble the image data, while an XOR operation with the encryption key was applied to randomize it. The main advantages of the proposed framework could be summarized as attaining a vast key space of 2^{2551} and a high encryption rate of 8.54 Mbps. Reaching such a key space is attributed to the usage of hyperchaotic functions, while the efficiency of the framework is attributed to the optimization of its software implementation and making use of parallel processing over six cores. Moreover, the proposed framework was tested against an array of security tests, both quantitative and qualitative in nature and was shown to exhibit comparable or even superior performance, in comparison to the state-of-the-art. Average achieved values for the quantitative metrics include MSE of 9626, PSNR of 8.3 dB, MAE of 80.99, entropy of 7.999, NPCR of 99.6% and UACI of 31.49%.

Future research efforts could be dedicated to attempting to improve the efficiency of the proposed image encryption framework even more. This could be carried out through an enhanced parallel processing architecture by running it over a network of connected machines or, better yet, by implementing it in hardware (i.e., on an FPGA, for example).

Author Contributions: Conceptualization, W.A., Y.-L.C. and L.Y.P.; methodology, W.A. and M.G.; software, W.A. and M.G.; validation, W.A.; writing—original draft preparation, W.A. and M.G.; writing—review and editing, W.A., Y.-L.C. and L.Y.P.; visualization, W.A.; supervision, W.A., Y.-L.C. and L.Y.P. All authors have read and agreed to the published version of the manuscript.

Funding: This research was funded by the National Science and Technology Council in Taiwan, grant number NSTC-109-2628-E-027-004–MY3, NSTC-111-2218-E-027-003 and NSTC-111-2622-8-027-009 and the Ministry of Education of Taiwan, official document number 1112303249.

Data Availability Statement: Not applicable.

Conflicts of Interest: The authors declare no conflict of interest.

Abbreviations

The following abbreviations are used in this manuscript:

CA	Cellular Automata
DNA	Deoxyribonucleic acid
HVS	Human Visual System
MAE	Maximum absolute error
MSE	Mean Square Error
NIST	National Institute of Standards and Technology
NPCR	Number of Pixel Changing Ratio
PRNG	Pseudo-Random Number Generation
PSNR	Peak Signal-to-Noise Ratio
S-box	Substitution box
SNM	Single Neuron Model
SPN	Substitution-Permutation Network
UACI	Unified Averaged Change Intensity

References

1. Hosny, K.M.; Kamal, S.T.; Darwish, M.M. A color image encryption technique using block scrambling and chaos. *Multimed. Tools Appl.* **2022**, *81*, 505–525. [CrossRef]
2. Alexan, W.; Elkandoz, M.; Mashaly, M.; Azab, E.; Aboshousha, A. Color Image Encryption through Chaos and KAA Map. *IEEE Access* **2023**, *11*, 11541–11554. [CrossRef]

3. Alexan, W.; Mamdouh, E.; ElBeltagy, M.; Ashraf, A.; Moustafa, M.; Al-Qurashi, H. Social Engineering and Technical Security Fusion. In Proceedings of the 2022 International Telecommunications Conference (ITC-Egypt), Alexandria, Egypt, 26–28 July 2022; pp. 1–5.
4. Jasra, B.; Moon, A.H. Color image encryption and authentication using dynamic DNA encoding and hyper chaotic system. *Expert Syst. Appl.* **2022**, *206*, 117861. [CrossRef]
5. Fang, J.; Jiang, M.; Yin, N.; Wei, D.; Zhang, Y. An image block encryption algorithm based on hyperchaotic system and DNA encoding. *Multimed. Tools Appl.* **2022**, *81*, 17245–17262. [CrossRef]
6. Alexan, W.; ElBeltagy, M.; Aboshousha, A. Rgb image encryption through cellular automata, s-box and the lorenz system. *Symmetry* **2022**, *14*, 443. [CrossRef]
7. Gabr, M.; Younis, H.; Ibrahim, M.; Alajmy, S.; Khalid, I.; Azab, E.; Elias, R.; Alexan, W. Application of DNA Coding, the Lorenz Differential Equations and a Variation of the Logistic Map in a Multi-Stage Cryptosystem. *Symmetry* **2022**, *14*, 2559. [CrossRef]
8. Gabr, M.; Alexan, W.; Moussa, K.; Maged, B.; Mezar, A. Multi-Stage RGB Image Encryption. In Proceedings of the 2022 International Telecommunications Conference (ITC-Egypt), Alexandria, Egypt, 26–28 July 2022; pp. 1–6.
9. Shannon, C.E. Communication theory of secrecy systems. *Bell Syst. Tech. J.* **1949**, *28*, 656–715. [CrossRef]
10. Elqusy, A.S.; Essa, S.E.; El-Sayed, A. Key management techniques in wireless sensor networks. *Commun. Appl. Electron. (CAE)* **2017**, *7*, 8–18.
11. Shariatzadeh, M.; Rostami, M.J.; Eftekhari, M. Proposing a novel Dynamic AES for image encryption using a chaotic map key management approach. *Optik* **2021**, *246*, 167779. [CrossRef]
12. Alexan, W.; Alexan, N.; Gabr, M. Multiple-Layer Image Encryption Utilizing Fractional-Order Chen Hyperchaotic Map and Cryptographically Secure PRNGs. *Fractal Fract.* **2023**, *7*, 287. [CrossRef]
13. Alexan, W.; ElBeltagy, M.; Aboshousha, A. Image Encryption Through Lucas Sequence, S-Box and Chaos Theory. In Proceedings of the 2021 8th NAFOSTED Conference on Information and Computer Science (NICS), Hanoi, Vietnam, 21–22 December 2021; pp. 77–83.
14. Matouk, A.; Lahcene, B. Rich complex dynamics in new fractional-order hyperchaotic systems using a modified Caputo operator based on the extended Gamma function. *Partial. Differ. Equ. Appl. Math.* **2022**, *6*, 100458. [CrossRef]
15. Younas, I.; Khan, M. A new efficient digital image encryption based on inverse left almost semi group and Lorenz chaotic system. *Entropy* **2018**, *20*, 913. [CrossRef]
16. Alexan, W.; ElBeltagy, M.; Aboshousha, A. Lightweight image encryption: Cellular automata and the lorenz system. In Proceedings of the 2021 International Conference on Microelectronics (ICM), New Cairo City, Egypt, 19–22 December 2021; pp. 34–39.
17. Elkandoz, M.T.; Alexan, W. Image encryption based on a combination of multiple chaotic maps. *Multimed. Tools Appl.* **2022**, *81*, 25497–25518. [CrossRef]
18. ElBeltagy, M.; Alexan, W.; Elkhamry, A.; Moustafa, M.; Hussein, H.H. Image Encryption through Rössler System, PRNG S-Box and Recamán's Sequence. In Proceedings of the 2022 IEEE 12th Annual Computing and Communication Workshop and Conference (CCWC), Las Vegas, NV, USA, 26–29 January 2022; pp. 0716–0722.
19. Iqbal, N.; Naqvi, R.A.; Atif, M.; Khan, M.A.; Hanif, M.; Abbas, S.; Hussain, D. On the Image Encryption Algorithm Based on the Chaotic System, DNA Encoding and Castle. *IEEE Access* **2021**, *9*, 118253–118270. [CrossRef]
20. ur Rehman, A.; Liao, X.; Ashraf, R.; Ullah, S.; Wang, H. A color image encryption technique using exclusive-OR with DNA complementary rules based on chaos theory and SHA-2. *Optik* **2018**, *159*, 348–367. [CrossRef]
21. Yang, B.; Liao, X. A new color image encryption scheme based on logistic map over the finite field ZN. *Multimed. Tools Appl.* **2018**, *77*, 21803–21821. [CrossRef]
22. Wang, Y.; Wu, C.; Kang, S.; Wang, Q.; Mikulovich, V. Multi-channel chaotic encryption algorithm for color image based on DNA coding. *Multimed. Tools Appl.* **2020**, *79*, 18342. [CrossRef]
23. Zhang, Y.Q.; He, Y.; Li, P.; Wang, X.Y. A new color image encryption scheme based on 2DNLCML system and genetic operations. *Opt. Lasers Eng.* **2020**, *128*, 106040. [CrossRef]
24. Jithin, K.; Sankar, S. Colour image encryption algorithm combining, Arnold map, DNA sequence operation and a Mandelbrot set. *J. Inf. Secur. Appl.* **2020**, *50*, 102428. [CrossRef]
25. Rehman, A.U.; Firdous, A.; Iqbal, S.; Abbas, Z.; Shahid, M.M.A.; Wang, H.; Ullah, F. A Color Image Encryption Algorithm Based on One Time Key, Chaos Theory and Concept of Rotor Machine. *IEEE Access* **2020**, *8*, 172275–172295. [CrossRef]
26. Li, B.; Liao, X.; Jiang, Y. A novel image encryption scheme based on logistic map and dynatomic modular curve. *Multimed. Tools Appl.* **2018**, *77*, 8911–8938. [CrossRef]
27. Hu, X.; Wei, L.; Chen, W.; Chen, Q.; Guo, Y. Color image encryption algorithm based on dynamic chaos and matrix convolution. *IEEE Access* **2020**, *8*, 12452–12466. [CrossRef]
28. Zhang, X.; Wang, L.; Wang, Y.; Niu, Y.; Li, Y. An image encryption algorithm based on hyperchaotic system and variable-step Josephus problem. *Int. J. Opt.* **2020**, *2020*, 6102824. [CrossRef]
29. Gong, L.; Qiu, K.; Deng, C.; Zhou, N. An image compression and encryption algorithm based on chaotic system and compressive sensing. *Opt. Laser Technol.* **2019**, *115*, 257–267. [CrossRef]
30. Lai, Q.; Hu, G.; Erkan, U.; Toktas, A. A novel pixel-split image encryption scheme based on 2D Salomon map. *Expert Syst. Appl.* **2023**, *213*, 118845. [CrossRef]
31. Erkan, U.; Toktas, A.; Lai, Q. 2D hyperchaotic system based on Schaffer function for image encryption. *Expert Syst. Appl.* **2023**, *213*, 119076. [CrossRef]

32. Song, W.; Fu, C.; Zheng, Y.; Tie, M.; Liu, J.; Chen, J. A parallel image encryption algorithm using intra bitplane scrambling. *Math. Comput. Simul.* **2023**, *204*, 71–88. [CrossRef]
33. Li, C.; Chen, G. Coexisting chaotic attractors in a single neuron model with adapting feedback synapse. *Chaos Solitons Fractals* **2005**, *23*, 1599–1604. [CrossRef]
34. Qi, G.; van Wyk, B.J.; van Wyk, M.A. A four-wing attractor and its analysis. *Chaos Solitons Fractals* **2009**, *40*, 2016–2030. [CrossRef]
35. Cui, N.; Li, J. A new 4D hyperchaotic system and its control. *AIMS Math.* **2023**, *8*, 905–923. [CrossRef]
36. Yang, Q.; Zhu, D.; Yang, L. A new 7D hyperchaotic system with five positive Lyapunov exponents coined. *Int. J. Bifurc. Chaos* **2018**, *28*, 1850057. [CrossRef]
37. Bassham, L.E.I.; Rukhin, A.L.; Soto, J.; Nechvatal, J.R.; Smid, M.E.; Barker, E.B.; Leigh, S.D.; Levenson, M.D.; Vangel, M.; Banks, D.L.; et al. *A Statistical Test Suite for Random and Pseudorandom Number Generators for Cryptographic Applications*; Revised 800-22; National Institute of Standards and Technology: Boulder, CO, USA, 2010.
38. Khan, M.; Masood, F. A novel chaotic image encryption technique based on multiple discrete dynamical maps. *Multimed. Tools Appl.* **2019**, *78*, 26203–26222. [CrossRef]
39. Khan, M.; Shah, T. An efficient chaotic image encryption scheme. *Neural Comput. Appl.* **2015**, *26*, 1137–1148. [CrossRef]
40. Liu, H.; Zhao, B.; Huang, L. Quantum image encryption scheme using Arnold transform and S-box scrambling. *Entropy* **2019**, *21*, 343. [CrossRef]
41. Wu, Y.; Noonan, J.; Agaian, S. NPCR and UACI randomness tests for image encryption. *Cyber J. Multidiscip. J. Sci. Technol. J. Sel. Areas Telecommun. (JSAT)* **2011**, *1*, 31–38.
42. Slimane, N.B.; Aouf, N.; Bouallegue, K.; Machhout, M. A novel chaotic image cryptosystem based on DNA sequence operations and single neuron model. *Multimed. Tools Appl.* **2018**, *77*, 30993–31019. [CrossRef]
43. Paul, L.; Gracias, C.; Desai, A.; Thanikaiselvan, V.; Suba Shanthini, S.; Rengarajan, A. A novel colour image encryption scheme using dynamic DNA coding, chaotic maps and SHA-2. *Multimed. Tools Appl.* **2022**, *81*, 37873–37894. [CrossRef]
44. Wu, X.; Kurths, J.; Kan, H. A robust and lossless DNA encryption scheme for color images. *Multimed. Tools Appl.* **2018**, *77*, 12349–12376. [CrossRef]
45. Alvarez, G.; Li, S. Some basic cryptographic requirements for chaos-based cryptosystems. *Int. J. Bifurc. Chaos* **2006**, *16*, 2129–2151. [CrossRef]
46. Asuero, A.G.; Sayago, A.; González, A. The correlation coefficient: An overview. *Crit. Rev. Anal. Chem.* **2006**, *36*, 41–59. [CrossRef]
47. Mahmood Malik, M.S.; Ali, M.A.; Khan, M.A.; Ehatisham-Ul-Haq, M.; Shah, S.N.M.; Rehman, M.; Ahmad, W. Generation of Highly Nonlinear and Dynamic AES Substitution-Boxes (S-Boxes) Using Chaos-Based Rotational Matrices. *IEEE Access* **2020**, *8*, 35682–35695. [CrossRef]
48. Hosny, K.M.; Kamal, S.T.; Darwish, M.M. Novel encryption for color images using fractional-order hyperchaotic system. *J. Ambient. Intell. Humaniz. Comput.* **2022**, *13*, 973–988. [CrossRef]
49. Zahid, A.H.; Arshad, M.J.; Ahmad, M. A novel construction of efficient substitution-boxes using cubic fractional transformation. *Entropy* **2019**, *21*, 245. [CrossRef]
50. Hayat, U.; Azam, N.A.; Asif, M. A method of generating 8×8 substitution boxes based on elliptic curves. *Wirel. Pers. Commun.* **2018**, *101*, 439–451. [CrossRef]
51. Siddiqui, N.; Yousaf, F.; Murtaza, F.; Ehatisham-ul-Haq, M.; Ashraf, M.U.; Alghamdi, A.M.; Alfakeeh, A.S. A highly nonlinear substitution-box (S-box) design using action of modular group on a projective line over a finite field. *PLoS ONE* **2020**, *15*, e0241890. [CrossRef]